


Spectra and structure functions of the temperature and velocity fields in supergravitational thermal turbulence ^F

Cite as: Phys. Fluids **34**, 055108 (2022); <https://doi.org/10.1063/5.0091012>

Submitted: 10 March 2022 • Accepted: 16 April 2022 • Accepted Manuscript Online: 19 April 2022 • Published Online: 04 May 2022

 Dongpu Wang,  Shuang Liu,  Quan Zhou, et al.

COLLECTIONS

 This paper was selected as Featured



View Online



Export Citation



CrossMark

ARTICLES YOU MAY BE INTERESTED IN

[Swimming of an inertial squirmer array in a Newtonian fluid](#)

Physics of Fluids **34**, 053303 (2022); <https://doi.org/10.1063/5.0090898>

[Perimeter leakage of face masks and its effect on the mask's efficacy](#)

Physics of Fluids **34**, 051902 (2022); <https://doi.org/10.1063/5.0086320>

[On the generation and destruction mechanisms of arch vortices in urban fluid flows](#)

Physics of Fluids **34**, 051702 (2022); <https://doi.org/10.1063/5.0088305>

APL Machine Learning

Open, quality research for the networking communities

MEET OUR NEW EDITOR-IN-CHIEF

LEARN MORE



Spectra and structure functions of the temperature and velocity fields in supergravitational thermal turbulence

Cite as: Phys. Fluids **34**, 055108 (2022); doi: [10.1063/5.0091012](https://doi.org/10.1063/5.0091012)

Submitted: 10 March 2022 · Accepted: 16 April 2022 ·

Published Online: 4 May 2022



View Online



Export Citation



CrossMark

Dongpu Wang,¹  Shuang Liu,^{1,2}  Quan Zhou,^{3,a)}  and Chao Sun^{1,4,a)} 

AFFILIATIONS

¹Center for Combustion Energy, Key Laboratory for Thermal Science and Power Engineering of MoE, and Department of Energy and Power Engineering, Tsinghua University, Beijing 100084, China

²Yau Mathematical Sciences Center, Tsinghua University, Beijing 100084, China

³Shanghai Key Laboratory of Mechanics in Energy Engineering, Shanghai Institute of Applied Mathematics and Mechanics, School of Mechanics and Engineering Science, Shanghai University, Shanghai 200072, China

⁴Department of Engineering Mechanics, School of Aerospace Engineering, Tsinghua University, Beijing 100084, China

^{a)} Author to whom correspondence should be addressed: qzhou@shu.edu.cn or chaosun@tsinghua.edu.cn

ABSTRACT

We analyze the power spectra and structure functions (SFs) of the temperature and radial velocity fields, calculated in the radial and azimuthal directions, in annular centrifugal Rayleigh–Bénard convection (ACRBC) for Rayleigh number $Ra \in [10^8, 10^{11}]$, Prandtl number $Pr = 10.7$, and inverse Rossby number $Ro^{-1} = 16$ using the spatial data obtained by quasi-two-dimensional direct numerical simulation. Bolgiano and Obukhov-like (BO59-like) scalings for the energy spectrum in both the azimuthal and radial directions and thermal spectrum in the azimuthal direction are observed. The range of BO59-like scaling becomes wider as Ra increases. At $Ra = 10^{11}$, it is found that BO59-like scaling $E_u(k_r) \sim k_r^{-11/5}$ spans nearly two decades for the energy spectrum calculated in the radial direction. Power-law fittings in the range larger than the Bolgiano scales, the scaling exponents of transverse and longitudinal velocity SFs vs the order coincide with the theoretical prediction of BO59 scaling $\zeta_p^u = 3p/5$ basically. The second-order temperature SFs exhibit a gradual transition from the Obukhov–Corrsin behavior at scales smaller than the Bolgiano scales to the BO59 behavior at scales larger than the Bolgiano scales. The slopes from the third to sixth-order temperature SFs are similar, which is similar to classical Rayleigh–Bénard convection and Rayleigh–Taylor turbulence. The probability density functions (p.d.f.) of temperature fluctuations $\delta T/\sigma_T$ reveal the cold plumes are strong and the p.d.f. in different regions at high Ra are similar. The stronger turbulent-mixing and larger centrifugal buoyancy in ACRBC may result in the BO59-like scaling.

Published under an exclusive license by AIP Publishing. <https://doi.org/10.1063/5.0091012>

I. INTRODUCTION

Turbulent convection is omnipresent in nature as well as in many engineering settings. Examples include circulations in the atmosphere^{1,2} and oceans^{3,4} driven by temperature differences, the convective flows in the Earth's mantle⁵ and outer core,⁶ and in some particular situations of rapidly rotating machines.^{7,8} An idealized model to study this type of flow is Rayleigh–Bénard convection (RBC), where a fluid is confined between two horizontal plates heated from below and cooled from above.^{9–19} An important issue for thermal turbulence studies is the influence of buoyancy on the small-scale dynamics.^{20,21} Recently, annular centrifugal RBC (ACRBC) system, where a

fluid is confined between two co-rotating cylinders heated from outside and cooled from inside, has been introduced to study turbulent convection.^{22–24} Through rapid rotation of the system, the centrifugal buoyancy is much larger than the Earth's gravity, around 100 times Earth's gravity in the laboratory experiments of Jiang *et al.*²⁵ The detection of the buoyancy-dominated energy cascade may be easier. Furthermore, Kunnen *et al.*²⁶ suggested that the structure function (SF) scalings could be longer for a larger-aspect-ratio cell since the separations between the different length scales may become larger. The larger azimuthal length of ACRBC than traditional RBC may increase the integral length scale. In addition, the effect of the proximity of the

sidewalls is avoided in ACRBC. In addition, the influence of rotation in addition to buoyancy often plays an important role in many convection phenomena.^{27–31} Thus, an exploration of the small-scale properties in ACRBC is needed.

The seminal work of the statistical properties of turbulence is Kolmogorov's theory³² for homogeneous and isotropic turbulence. Kolmogorov³² considered that the kinetic energy only injects at integral scales and cascades down to dissipative scales. This energy cascade range is the so-called inertial range. The well-known scaling (K41) for the second-order velocity SF $S_2(\mathbf{r}) = \langle [u(\mathbf{x} + \mathbf{r}) - u(\mathbf{x})]^2 \rangle_{\mathbf{x},t} \sim (\varepsilon_u r)^{2/3}$ was derived, where u is one component of the velocity, \mathbf{x} is a position coordinate, \mathbf{r} is the separation vector and $r \equiv |\mathbf{r}|$, $\langle \cdots \rangle_{\mathbf{x},t}$ denotes an average over the space and time, and ε_u is the mean energy dissipation rate. The corresponding scaling exponents for the p th-order velocity SFs is $S_p(\mathbf{r}) \sim r^{p/3}$. Applying Fourier transform to the two-point correlation $\langle \mathbf{u}(\mathbf{x}, t) \cdot \mathbf{u}(\mathbf{x} + \mathbf{r}, t) \rangle$, the corresponding energy spectrum has a scaling of $E_u(k) \sim k^{-5/3}$, where k is the wavenumber. Extending the Kolmogorov's theory, Obukhov³³ and Corrsin³⁴ deduced a universal scaling (OC) of the passive scalar spectrum $E_\theta(k) \sim k^{-5/3}$ and the corresponding SFs $R_p(\mathbf{r}) \sim r^{p/3}$.

For thermal turbulence, temperature can modify the velocity field through the buoyancy force and the flow becomes anisotropic. In stably stratified turbulence, Bolgiano³⁵ and Obukhov³⁶ independently derived the scalings (BO59) $E_u(k) \sim k^{-11/5}$ for energy spectrum and $E_\theta(k) \sim k^{-7/5}$ for thermal spectrum in the buoyancy subrange $1/L_0 \ll k \ll 1/L_B$. Here, L_0 is the integral length scale. L_B is the so-called Bolgiano length,^{35,36}

$$L_B = \varepsilon_u^{5/4} \varepsilon_\theta^{-3/4} (\alpha g)^{-3/2}, \quad (1)$$

where ε_θ is the mean thermal dissipation rate, α is the thermal expansion coefficient, and g is the gravitational acceleration. For $L_B \ll r \ll L_0$, the corresponding scalings of the p th-order velocity and temperature SFs are $S_p(\mathbf{r}) \sim r^{3p/5}$ and $R_p(\mathbf{r}) \sim r^{p/5}$, respectively. For $\eta_K \ll r \ll L_B$, the scalings of spectra and SFs return back to K41 and OC laws, where η_K is the Kolmogorov length scale. For a detailed derivation of these scalings, one can refer to Monin and Yaglom.³⁷ Later, it was proven that BO59 scalings are also applicable for convective turbulence.^{38,39} Assuming spatial homogeneity, the rigorous relations for ε_u and ε_θ can be derived. Combining Eq. (1), one can obtain the global-averaged Bolgiano scale,

$$L_B = \frac{\text{Nu}^{1/2} L}{(\text{RaPr})^{1/4}}, \quad (2)$$

where the Nusselt number (Nu) is the total heat flux normalized by the conductive flux (the definitions of the dimensionless parameters are provided in Sec. II), the Rayleigh number (Ra) characterizes the buoyancy-driven strength, the Prandtl number (Pr) reflects the ratio of the viscous dissipation and thermal diffusivity, and L is the characterized length of the flow domain.

While identifying BO59 scaling is challenging. First, the separation between L_B and L_0 needs to be large. Moreover, the inhomogeneity of the RBC leads to the assumption of BO59 scaling being not very exact, for example, the time-averaged ε_u and ε_θ are strong at the hot and cold plates.^{26,40,41} Furthermore, the shear effect of the large-scale circulation (LSC) results in a scaling of the shear flow,⁴² which is

approximate to the scaling of BO59 laws. Intermittency effects existing in RBC also cause the issue more complicated.^{43,44} In addition, the single-point statistical method is doubtful since the Taylor hypothesis⁴⁵ is often not met in RBC,^{46,47} while high-resolution simultaneous multipoint measurements are difficult for experiments.^{26,48–50}

Nevertheless, there has been a lot of work on the discussion of the existence of the BO59 scaling, and this issue is still under debate in the field. Wu *et al.*⁵¹ found a BO59 scaling using the single-point temperature measurements in a helium-gas cell. Tong and Shen⁵² conducted preliminary multipoint measurements by the photon-correlation homodyne spectroscopy method and found the BO59 scaling of velocity fluctuations. Evidence of BO59 scaling on the temperature has been available for some studies,^{51,53–58} while velocity scaling is more elusive.^{57,59,60} Kunnen *et al.*²⁶ computed the SFs up to fourth-order using spatial data obtained by direct numerical simulation (DNS) and experiments, and they observed BO59 scaling for both velocity and temperature. Rosenberg *et al.*⁶¹ found evidence for BO59 scaling in rotating stratified turbulence using DNS. Additionally, BO59 scaling is validated in another buoyancy-induced flow, two-dimensional Rayleigh–Taylor turbulence.^{62–64} On the other hand, some researchers have argued in favor of the K41 and OC scalings. Sun *et al.*⁴⁹ experimentally addressed that K41 and OC scalings are valid for the flow in the central region of the cell. Zhou and Xia⁶⁵ disentangled the anisotropies produced by the thermal plumes and found that the part of velocity SF which excludes the contribution of plumes exhibits K41 scalings, while the other part which includes the effect of plumes deviates from K41. Kaczorowski and Xia⁶⁶ showed that the longitudinal velocity increments approach a K41-like scaling in the bulk region by simulations. Recently, Bhattacharya *et al.*⁶⁷ also argued that the kinetic-energy spectrum is Kolmogorov-like for a flow with $\text{Pr} \lesssim 1$.

In this paper, using the temperature and velocity field data of quasi-two-dimensional DNS, it is unprecedentedly able to identify the BO59-like scalings in high-Ra ACRBC. At $\text{Ra} = 10^{11}$, BO59-like scaling $E_u(k_r) \sim k_r^{-11/5}$ spanning nearly two decades for the energy spectrum calculated in the radial direction is observed. The remainder of this manuscript is organized as follows. In Sec. II, we give a brief description of the numerical arrangement, including the governing equations, the parameters and resolution settings, and the process of the calculation of the spectra and SFs. The results are presented and analyzed in Sec. III, which is divided into three parts, Sec. III A describes the thermal spectra and energy spectra. In Sec. III B, we show the temperature and radial velocity SFs calculated in the azimuthal and radial directions. The probability density functions (p.d.f.s) of the temperature fluctuations in different regions are examined in Sec. III C. In Sec. IV, we provide a discussion about the new features in ACRBC. Finally, we summarize our findings in Sec. V.

II. NUMERICAL ARRANGEMENT

A. Parameter descriptions

DNS concerns the flow in a cylindrical annulus with cold inner and hot outer walls corotating axially [see Fig. 1(a)]. The flow inside this volume is governed by the Boussinesq equations in a rotating reference frame,

$$\nabla \cdot \mathbf{u} = 0, \quad (3)$$

$$\frac{D\theta}{Dt} = \frac{1}{\sqrt{\text{RaPr}}} \nabla^2 \theta, \quad (4)$$

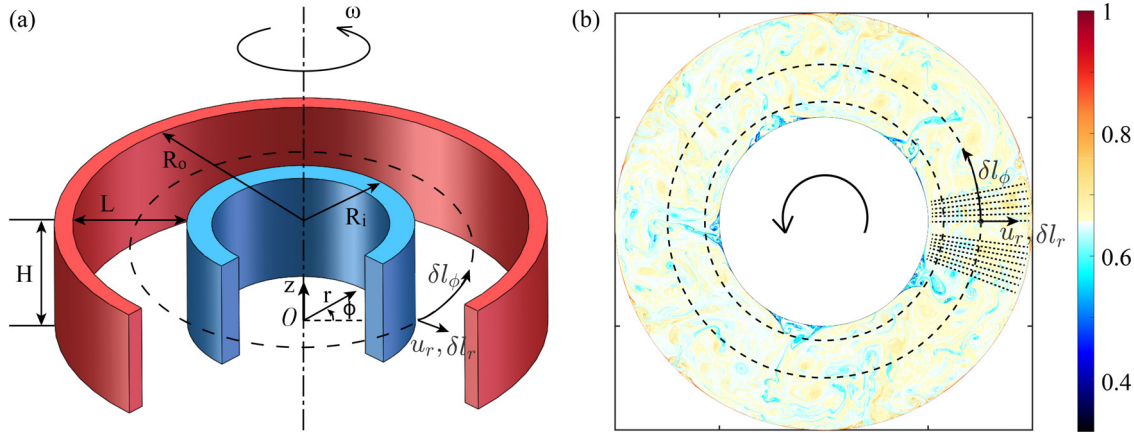


FIG. 1. Flow setup and temperature snapshot. (a) Sketch of the system, which defines the cylindrical coordinates and parameters. (b) Instantaneous temperature field at $z/H = 0.5$ for $Ra = 10^{11}$. The large dashed circle denotes the first set of numerical probes inserted at the radial position $R' = (r - R_i)/L = 0.5$, along which the power spectra in the azimuthal direction are calculated. The small dashed circle with $R' = 0.15$, which approaches the inner cylinder but outside of the boundary layer, where the second set of probes are distributed and used to calculate the structure functions in the azimuthal direction. The dotted lines denote part of the third set of probes inserted in the bulk region (except the BLs) in which the power spectra and SFs in the radial direction are calculated. To visualize clearly, the dotted lines are plotted only in part of the azimuthal region. The colorbar is from 0.3 to 1. In (a) and (b), the directions of the radial velocity u_r , separations for the calculation of SFs δl_r and δl_ϕ are signified.

$$\frac{D\mathbf{u}}{Dt} = -\nabla p - Ro^{-1}\hat{\omega} \times \mathbf{u} + \sqrt{\frac{Pr}{Ra}}\nabla^2 \mathbf{u} - \theta \frac{2(1-\eta)}{(1+\eta)} \mathbf{r}. \quad (5)$$

Here \mathbf{u} , θ , and p are the dimensionless velocity vector, temperature, and pressure, respectively. D/Dt represents the material derivative. $\hat{\omega}$ is the unit vector pointing in the direction of the angular velocity. The equations have been made dimensionless with the gap width $L = R_o - R_i$, temperature difference $\Delta = T_{hot} - T_{cold}$, and the free fall velocity $U \equiv \sqrt{\omega^2[(R_o + R_i)/2]\alpha\Delta L}$. R_o and R_i are the radius of the outer and inner cylinders. T_{hot} and T_{cold} are the temperature of the outer and inner cylinders. ω denotes the angular velocity of the system.

From the governing equations, it is revealed that the control parameters of the system are the Rayleigh number,

$$Ra = \frac{1}{2}\omega^2(R_o + R_i)\alpha\Delta L^3/(\nu\kappa), \quad (6)$$

the Prandtl number $Pr = \nu/\kappa$, the inverse Rossby number (measuring Coriolis effects) $Ro^{-1} = \omega L/U$, the radius ratio $\eta = R_i/R_o$, and aspect ratios $\Gamma_\perp = H/L$ and $\Gamma_\parallel = 2\pi r/L$. Here, ν and κ are the kinematic viscosity and thermal diffusivity of the fluid, respectively. In the present study of small-scale statistics, the simulations are performed for Ra from 10^8 to 10^{11} for a fixed Pr of $Pr = 10.7$, a fixed inverse Rossby number of $Ro^{-1} = 16$, and a fixed η of $\eta = 0.5$. These parameter conditions (Pr , Ro^{-1} and η) are the same as our another experimental work studying the ultimate regime of thermal turbulence.²⁵ $Pr = 10.7$ corresponds to the Novec-7200 fluid at 25°C or water at 7°C . We also note that Γ_\parallel is dependent on η , the mean aspect ratio $\bar{\Gamma}_\parallel = \pi(R_o + R_i)/L = \pi(1 + \eta)/(1 - \eta)$. The key response parameter is the Nusselt number $Nu = J/J_{con} = -JR_o \ln \eta/(\lambda\Delta)$, where J and J_{con} denote the total heat flux and the heat flux through pure thermal conduction, respectively, and $\lambda = \kappa\rho c_p$ is the thermal conductivity of the working fluid with ρ and c_p the density and the specific heat capacity of the fluid, respectively.

B. Direct numerical simulations

Equations (3)–(5) are solved in cylindrical coordinates (ϕ, z, r) , where ϕ , z , and r refer to the streamwise (azimuthal), spanwise (axial), and wall-normal (radial) directions, respectively [see Fig. 1(a)]. No-slip and isothermal boundary conditions are imposed on the inner and outer cylindrical walls, periodic boundary conditions in the axial direction. Details of the numerical procedure can be referred to Verzicco and Orlandi⁶⁸ and Jiang *et al.*,²² here, we present an overview. The discretization adopts second-order finite-difference for the derivatives in space. Time advancement uses a fractional-step third-order Runge-Kutta scheme, and the maximum Courant number is 0.8. The simulation parameters and resolution settings for the calculation of spectra and SFs are summarized in Table I. The averaging time for simulations ranges from 14.9 to 190.4 free fall time (τ_{avg}) after reaching a steady state. The grid resolutions are varied from $N_\phi \times N_z \times N_r = 3072 \times 48 \times 256$ for $Ra = 10^8$ to $18432 \times 48 \times 1536$ for $Ra = 10^{11}$.

A representative temperature snapshot at the mid-axial position at $Ra = 10^{11}$ is provided in Fig. 1(b), giving an impression of the typical flow structures. The simulation for high Ra needs tremendous amount of CPU hours, and the flow exhibits quasi-2D state when Ro^{-1} is large.²² Thus, we conduct quasi-two-dimensional DNS, that is, the flow is constrained in a thin annular region. $\Gamma_\perp = H/L \sim 0.1$ for all cases (listed in Table I). The variation of the radial velocity $[(u_r)_{std}/\langle |u_r| \rangle_{z,t}]$ of the four cases presented in Table I is all very small ($\lesssim 10^{-4}$), where $(u_r)_{std}/\langle |u_r| \rangle_{z,t}$ is the standard deviation of the radial velocity u_r divided by $|u_r|$ averaged axially and by time at the azimuthal position of the maximum $|u_r|$. So the flow exhibits quasi-2D state in the quasi-2D convection cell. In addition, we note that the azimuthal region is not reduced for all cases in the present study. For example, $N_\phi = 18432$ means 18432 points for the whole azimuthal region (2π) of the annulus.

The maximum grid spacings Δ_g have been compared to the Kolmogorov scale η_K and the Batchelor scale $\eta_B = \eta_K/(Pr^{1/2})$. Here, $\eta_K = Pr^{1/2}[RaNu_f(\eta)]^{-1/4}L$ [Eq. (A10)] is based on the rigorous

TABLE I. Simulation parameters and resolution settings for the calculation of spectra and SFs. The columns from left to right indicate the followings: Rayleigh number Ra ; Nusselt number Nu ; $Diff_{Nu} \equiv |Nu - Nu_h|/Nu$ is used to evaluate the statistical convergence, where Nu_h is the counterpart of Nu , averaged over the second half of $Nu(t)$; the averaging time period τ_{avg} after the system has reached statistically stationary state; $(u_r)_{std}/\langle u_r \rangle_{z,t}$ is the standard deviation of the radial velocity u_r divided by u_r , averaged axially and by time at the azimuthal position of the maximum u_r , which is used to suggest the flow is in the quasi-2D flow state; the resolution in the azimuthal, radial, and axial directions $N_\phi \times N_r \times N_z$; the maximum grid spacing in the bulk region Δ_g compared with the Batchelor scale; the number of grid points within the viscous boundary layer (BL) N_{v-BL} and thermal BL N_{t-BL} near the outer cylinder; aspect ratio $\Gamma_\perp = H/L$; radius ratio $\eta = R_i/R_o$.

Ra	Nu	$Diff_{Nu}$	τ_{avg}	$(u_r)_{std}/\langle u_r \rangle_{z,t}$	$N_\phi \times N_r \times N_z$	Δ_g/η_B	N_{v-BL}	N_{t-BL}	Γ_\perp	η
10^8	25.30	0.83%	190.4	2.60×10^{-16}	$3072 \times 256 \times 48$	1.28	19	16	0.19	0.5
10^9	48.46	0.72%	116.7	5.48×10^{-8}	$6144 \times 512 \times 48$	1.37	34	25	0.09	0.5
4.7×10^{10}	143.18	0.76%	41.47	6.76×10^{-5}	$12\,288 \times 1024 \times 48$	2.39	40	31	0.05	0.5
10^{11}	180.38	0.85%	14.9	1.43×10^{-4}	$18\,432 \times 1536 \times 48$	2.06	56	42	0.05	0.5

relations for the volume and time-averaged kinetic and thermal dissipation rates. The derivation of η_K is provided in the Appendix. The resolution criterion for the bulk, $\Delta_g < \eta_K$ and $\Delta_g < 2.5\eta_B$, found to be adequate in Verzicco and Camussi⁶⁹ and Kunnen *et al.*,²⁶ is thus fulfilled. In addition, we check the bulk resolution by studying the scaling of the second-order transverse and longitudinal SFs, S_2^{T,u_r} and S_2^{L,u_r} , of the radial velocity u_r with separations δl in the dissipative range (The directions of δl are shown in Fig. 1). The velocity increments are averaged in the bulk region and over time. From Fig. 2, it is indicated that for both $Ra = 10^8$ and 10^{11} , $S_2^{T,u_r} \sim (\delta l_\phi)^2$ and $S_2^{L,u_r} \sim (\delta l_r)^2$, when δl is of the order of the Kolmogorov length scale η_K . The crossover scales between the dissipative range and the inertial range are about several times of η_K . In addition, it is found that $S_2^{T,u_r} \simeq S_2^{L,u_r}/2$ at $Ra = 10^{11}$. The results of second-order SFs in the dissipative range for ACRBC are similar to traditional RBC.⁶⁶ On the one hand, this suggests that the bulk resolution is adequate to resolve the dissipative scales; on the other hand, it also implies that the flow in the bulk region of ACRBC at $Ra = 10^{11}$ is nearly homogeneous and isotropic. As the BL near the outer cylinder is thinner than that near the inner cylinder,²⁴ there are at least 19 grid points inside viscous BL and 16 grid points inside thermal BL near the outer cylinder, so it is well-resolved. We validate our simulations by computing the Nu

averaged over the last half of the τ_{avg} range (Nu_h) and averaged over the entire τ_{avg} range (Nu) and ensuring that the deviation $Diff_{Nu} = |Nu - Nu_h|/Nu < 1\%$.^{23,67} Thus, a satisfactory statistical convergence is attained.

C. Methods for the calculation of the spectra and structure functions

Many numerical probes are distributed in the flow field. The probes are positioned at grid points and record the evolution of the temperature θ and radial velocity u_r at these grid points in time. As shown in Fig. 1(b), the first set of probes are distributed along the cylindrical surface with the radial position $R' = (r - R_i)/L = 0.5$. The data acquired from these $N_\phi(\times N_z)$ probes are used to calculate the power spectra (PS) $E_{\theta,u}(k_\phi)$ as a function of the azimuthal wave-number k_ϕ . Kunnen *et al.*²⁶ found local Bolgiano scale is small when approaching the walls but outside of the boundary layers (BLs), which can lead to longer BO59 scaling regime. Thus, the second set of probes are distributed along the surface near the inner cylinder with the radial position $R' = 0.15$. Temperature SFs in the azimuthal direction $R_p^\phi(\delta l_\phi) \equiv \langle |\theta(\mathbf{x} + \delta l_\phi) - \theta(\mathbf{x})|^p \rangle$ and transverse SFs for the radial velocity $S_p^{T,u_r}(\delta l_\phi) \equiv \langle |u_r(\mathbf{x} + \delta l_\phi) - u_r(\mathbf{x})|^p \rangle$ are calculated by this

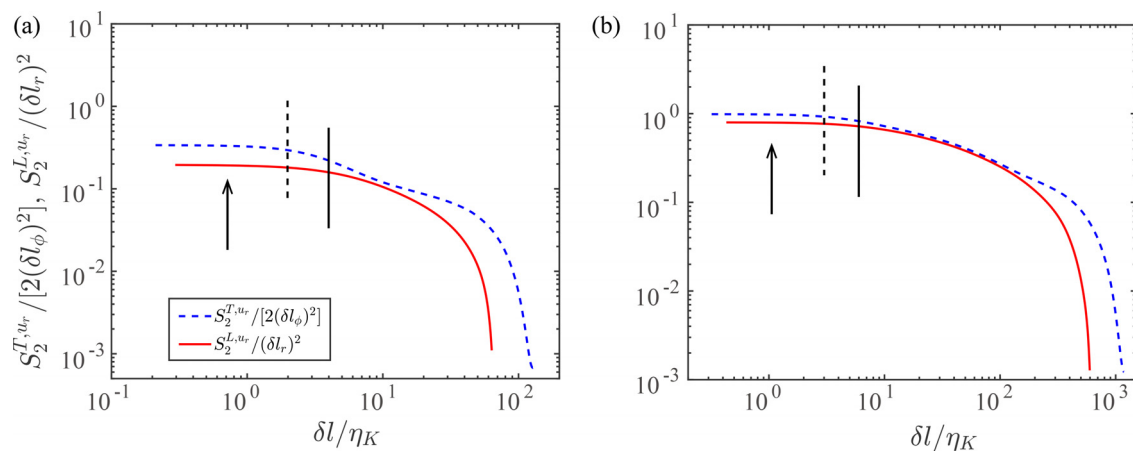


FIG. 2. Comparison of the second-order transverse structure function S_2^{T,u_r} with the second-order longitudinal structure function S_2^{L,u_r} plotted in compensated form for (a) $Ra = 10^8$, $Ro^{-1} = 16$, $Pr = 10.7$ and (b) $Ra = 10^{11}$, $Ro^{-1} = 16$, $Pr = 10.7$. The vertical lines denote the crossover scales between the dissipative range and the inertial range. The arrows mark the dissipative ranges, which are smaller than the crossover scales.

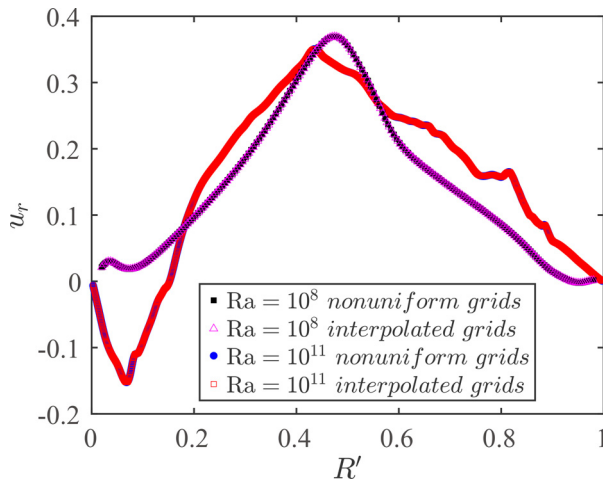


FIG. 3. Comparison of the instantaneous u_r profiles (except the BLs) adopted clipped Chebychev-type clustering grids with the interpolated grids with uniform separations at the mid-axial and an azimuthal position at $Ra = 10^8$, $Ro^{-1} = 16$, $Pr = 10.7$ and $Ra = 10^{11}$, $Ro^{-1} = 16$, $Pr = 10.7$. The deviations of the u_r are very small so the interpolation produce negligible effects on PS and SFs.

set of probe data. The PS and SFs in the azimuthal direction are averaged axially, azimuthally, and by time. In addition, the azimuthal domains are divided into 3, 7, 14, and 22 equal azimuthal parts for $Ra = [10^8, 10^9, 4.7 \times 10^{10}, 10^{11}]$, respectively. The PS and SFs are then averaged over the several azimuthal parts. As shown in Fig. 4, the maximum scale of the case with larger Ra is smaller since the azimuthal region is divided into more parts.

The third set of numerical probes are inserted into every radial profile distributed over 2π except the BLs, i.e., all grid points in the bulk region. This set of data are used to calculate PS $E_{\theta,u}(k_r)$ as a function of the radial wavenumber k_r , temperature SFs in the radial direction $R_r^T(\delta \mathbf{l}_r) \equiv \langle |\theta(\mathbf{x} + \delta \mathbf{l}_r) - \theta(\mathbf{x})|^2 \rangle$, and longitudinal SFs for the radial velocity $S_p^{L,u_r}(\delta \mathbf{l}_r) \equiv \langle |\mathbf{u}_r(\mathbf{x} + \delta \mathbf{l}_r) - \mathbf{u}_r(\mathbf{x})|^2 \rangle$. Note that PS and SFs in the radial direction are averaged axially, azimuthally, radially, and by time. We also note that since the clipped Chebychev-type clustering grids are adopted in the radial direction to ensure the spatial resolution within BLs, the grid positions are nonuniform for the third set

of probes. In order to average the PS and SFs in the radial direction, the velocity and temperature are first interpolated onto a uniform grid with a cubic spline interpolation algorithm separately for each azimuthal positions and each time step. We note that the deviations of the original value and the interpolated value are very small so the interpolation effects on the statistics are negligible (see Fig. 3). Then, spectra and SFs in the radial direction are calculated followed by space and time averaging. All the spectral quantities and SFs are averaged over at least 40 snapshots taken at $0.2t$ intervals after reaching a steady state.

III. RESULTS

A. Spectra

We discuss first about the characteristic scales. In the Appendix, we derive the two exact relations for kinetic and thermal dissipation rates in ACRBC, which are similar to those of classical RBC only with small radius ratio corrections. Thus, the characteristic scales of ACRBC are also approximately equal to those of classical RBC. Table II lists the Bolgiano scales L_B for each case. L_B decreases with the increase in Ra . Thus, the range of BO59 scaling should become wider for higher Ra .

We calculate the spectra both in the azimuthal and radial directions. Let us first examine the scaling properties of the power spectra calculated in the azimuthal direction. Figures 4(a) and 4(b) plot the PS vs the azimuthal wavenumber k_ϕ for temperature and radial velocity, respectively. At $3 \leq k_\phi \leq 50$ for $Ra \geq 10^9$, temperature PS display a scaling exponent around $-7/5$, i.e., the BO59-like scaling. This is particularly evident from the compensated spectra plotted in Fig. 4(c), while for larger wavenumber, the scaling range of $-5/3$ is very limited. For radial velocity spectra, we find a scaling of $E_u(k_\phi) \sim k_\phi^{-11/5}$ [also see Fig. 4(d)], which is the BO59 scaling for the energy spectrum. Similarly, no obvious K41 scaling [$E_u(k_\phi) \sim k_\phi^{-5/3}$] for larger wavenumbers follows. It is known that centrifugal buoyancy is in the radial direction, so we do not expect that energy cascade in the azimuthal direction will be modified by the buoyancy. Nevertheless, BO59-like scalings are found for the temperature and radial velocity spectra calculated in the azimuthal direction. We consider that might be due to the strong mixing effects of the LSC at high Ra .

In addition, the width of the wavenumber range over which BO59-like scaling is observed indeed increases with Ra : from $4 \leq k_\phi \leq 15$ at $Ra = 10^8$ to $3 \leq k_\phi \leq 80$ at $Ra = 10^{11}$ for the thermal

TABLE II. Global estimates of different length scales at different Ra . $(L_0)_{azi}$ and $(L_0)_{rad}$ are the transverse integral scale and longitudinal integral scale, which are calculated by the integration of the transverse and longitudinal autocorrelation functions of radial velocity u_r , respectively.⁷⁰ The Bolgiano scale $L_B = \frac{Nu^{1/2}L}{(PrRa)^{1/4}} [f(\eta)]^{1/2}$ and Kolmogorov scale $\eta_K = \frac{Pr^{1/2}L}{(RaNu)^{1/4}} [f(\eta)]^{-1/4}$ are based on the rigorous relations for the volume and time-averaged kinetic and thermal dissipation rates (the derivation is given in the Appendix). Here, the correction of radius ratio $f(\eta) = \frac{2(\eta-1)}{(1+\eta)\ln(\eta)}$ and the derivation of $f(\eta)$ are supplied in the Appendix. $(k_0)_{azi}$, $(k_0)_{rad}$, k_B , and k_η are the corresponding wavenumber of the length scales ($k = 1/L$).

Ra	$(L_0)_{azi}$	$(L_0)_{rad}$	$L_B (\times 10^{-2})$	$\eta_K (\times 10^{-2})$	$(k_0)_{azi}$	$(k_0)_{rad}$	k_B	k_η
10^8	0.147	0.178	2.73	1.47	6.81	5.61	35.67	68.84
10^9	0.133	0.148	2.12	0.70	7.54	6.75	46.22	143.40
4.7×10^{10}	0.096	0.128	1.39	0.21	10.44	7.82	71.17	489.63
10^{11}	0.081	0.119	1.30	0.16	12.29	8.40	75.81	629.69

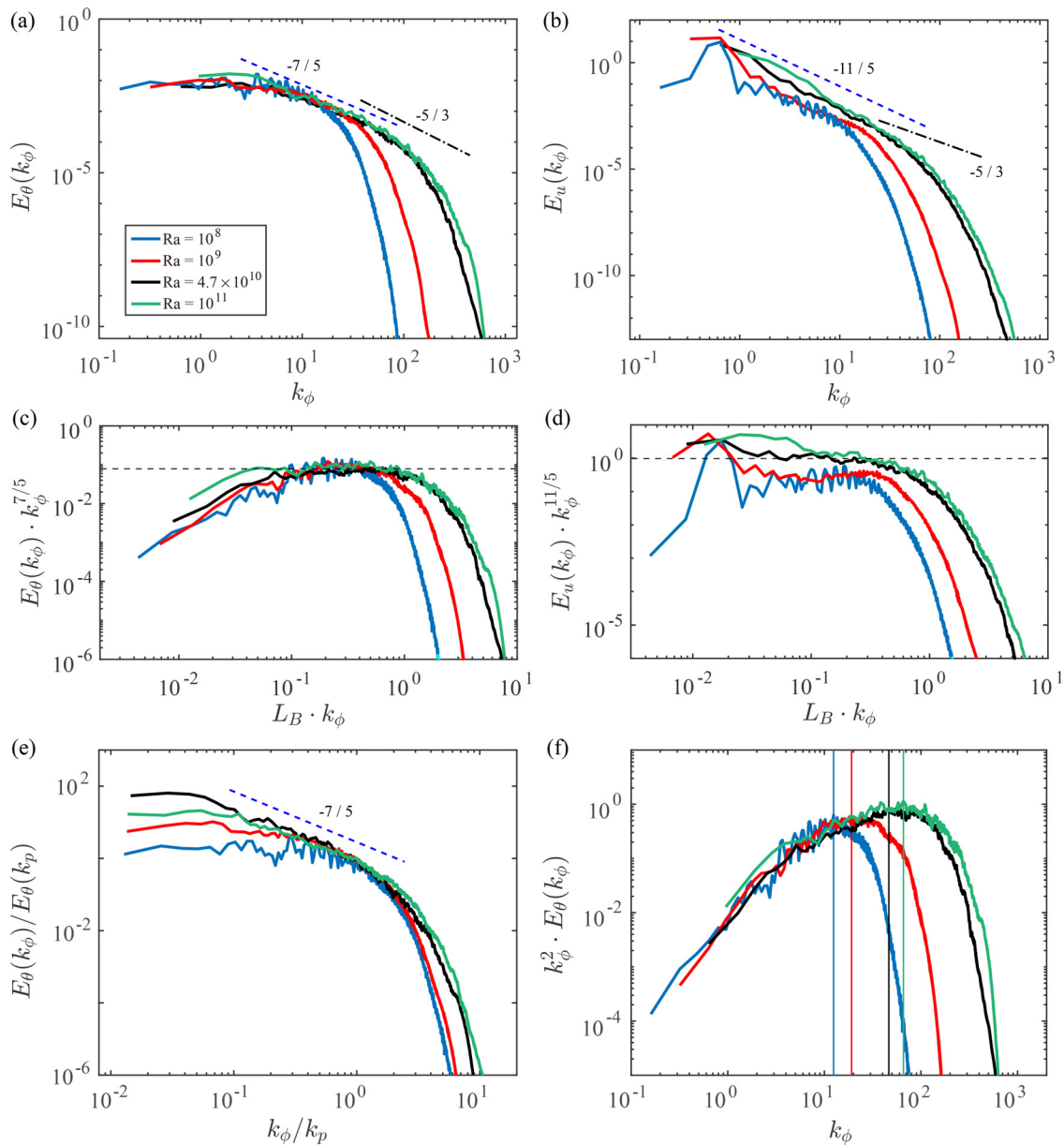


FIG. 4. (a) Temperature power spectra $E_\theta(k_\phi)$ as a function of the azimuthal wavenumber k_ϕ , averaged axially, azimuthally, and by time for different Ra . The maximum scales of the cases are slightly different because of the different lengths of azimuthally divided regions. (b) Radial velocity power spectra $E_u(k_\phi)$ as a function of the azimuthal wavenumber k_ϕ , averaged axially, azimuthally, and by time for different Ra . [(c) and (d)] Compensated plot of [(a) and (b)] with the PS compensated by the BO59 scaling prediction, and the azimuthal wavenumber k_ϕ compensated by the Bolgiano scale L_B . The horizontal dashed lines mark the BO59 scaling. (e) Temperature power spectra scaled by the energy $E_\theta(k_p)$ and the characteristic scale k_p . (f) Temperature dissipation spectra $k_\phi^2 \cdot E_\theta(k_\phi)$ for different Ra . The vertical lines are the positions of k_p , which are the peak wavenumbers of the corresponding dissipation spectra. All data are for the cylindrical surfaces at radial location $R' = (R - R_i)/L = 0.5$. All fractions are the slopes of the nearby reference lines.

spectra [Fig. 4(a)] and from $1 \leq k_\phi \leq 10$ at $Ra = 10^8$ to $1 \leq k_\phi \leq 30$ at $Ra = 10^{11}$ for the energy spectra [Fig. 4(b)]. As shown in the compensated Figs. 4(c) and 4(d), the compensated PS are flat at $L_B \cdot k_\phi \lesssim 1$, which means the ranges of BO59 scalings are basically consistent with the theoretical predictions ($k_0 \leq k \leq k_B$) listed in Table II. Furthermore, Zhou and

Xia⁵⁸ identified the “Bolgiano frequency” as the peak frequency of the dissipation spectra and found a universal BO59 range for different Ra . We calculate the wavenumber k_p corresponding to the maximum value of the temperature dissipation spectrum $k_\phi^2 \cdot E_\theta(k_\phi)$ [see Fig. 4(f)]. It is found that k_p increases with the increase in Ra . Normalized by this characteristic

wavenumber, PS for different Ra are basically collapsed in the mesoscale [Fig. 4(e)] and obey around $-7/5$ scaling relation at $Ra \geq 4.7 \times 10^{10}$.

In addition, it is observed that the amplitude of the energy spectrum increases with Ra [Fig. 4(b)], which suggests that convection with large Ra has more kinetic energy than that with small Ra. Note that the spectrum exhibits strong fluctuations at the intermediate wavenumbers at $Ra = 10^8$ and gradually becomes smooth at higher Ra. That may be because for high Ra, the flow is more turbulent and the nonlinear interactions among the modes become more intense. While at $Ra = 10^8$, the more coherent thermal plumes possibly induce the fluctuations of energy.

Next, we examine temperature and radial velocity PS calculated in the radial direction. Since centrifugal buoyancy affects the turbulent flow moving along the radial direction more directly, buoyancy will feed kinetic energy and may alter the energy cascade. While as shown in Figs. 5(a) and 5(c), there exists no more than one decade scaling range for temperature PS in the radial direction. For radial velocity PS calculated in the radial direction [Fig. 5(b)], BO59-like scaling for the energy spectrum is identified. The scaling $-11/5$ is observed for each Ra, and this significant scaling regime spans nearly two decades from $k_r \sim 2$ to $k_r \sim 200$ for $Ra \geq 4.7 \times 10^{10}$. The flat region of Fig. 5(d) occurs at $L_B \cdot k_r \lesssim 1$, which indicates that the BO59-like scaling is observed for $k_r \lesssim k_B$. In ACRBC, the radial velocity spectra follow BO59-like scaling, which suggests the energy cascade in the inertia

range is influenced by centrifugal buoyancy. Later it is confirmed that the corresponding scaling exponents ζ_p^u for the p th-order radial velocity SFs also possibly follow the relation of BO59 scaling $\zeta_p^u = 3p/5$.

B. Structure functions

In this part, the temperature and radial velocity SFs calculated in the azimuthal and radial directions will be discussed. As Kunnen *et al.*²⁶ reported, the local Bolgiano scale is smaller when approaching the hot or cold walls, but outside of the boundary layers. Hence, to observe a longer range of BO59 scaling, the radial position of the SFs calculated in the azimuthal direction is at $R' = 0.15$, which is near the inner cylinder while out of the BL. Temperature SFs in the azimuthal direction and transverse SFs for the radial velocity are defined as $R_p^\phi(\delta l_\phi) \equiv \langle |\theta(\mathbf{x} + \delta \mathbf{l}_\phi) - \theta(\mathbf{x})|^p \rangle$ and $S_p^{T,u_r}(\delta l_\phi) \equiv \langle |\mathbf{u}_r(\mathbf{x} + \delta \mathbf{l}_\phi) - \mathbf{u}_r(\mathbf{x})|^p \rangle$, respectively. The SFs in the azimuthal direction are averaged axially, azimuthally, and by time. Similarly, temperature SFs in the radial direction and longitudinal SFs for the radial velocity are calculated by $R_p^r(\delta l_r) \equiv \langle |\theta(\mathbf{x} + \delta \mathbf{l}_r) - \theta(\mathbf{x})|^p \rangle$ and $S_p^{L,u_r}(\delta l_r) \equiv \langle |\mathbf{u}_r(\mathbf{x} + \delta \mathbf{l}_r) - \mathbf{u}_r(\mathbf{x})|^p \rangle$, respectively. The SFs in the radial direction are averaged axially, azimuthally, radially, and by time.

Let us first discuss the temperature SFs. The scaling of the temperature SFs is not obvious (Fig. 6). We show the 1–6 order temperature SFs at $Ra = 10^{11}$ in Figs. 6(a) and 6(b). For $\delta l \geq L_B$, the slope for

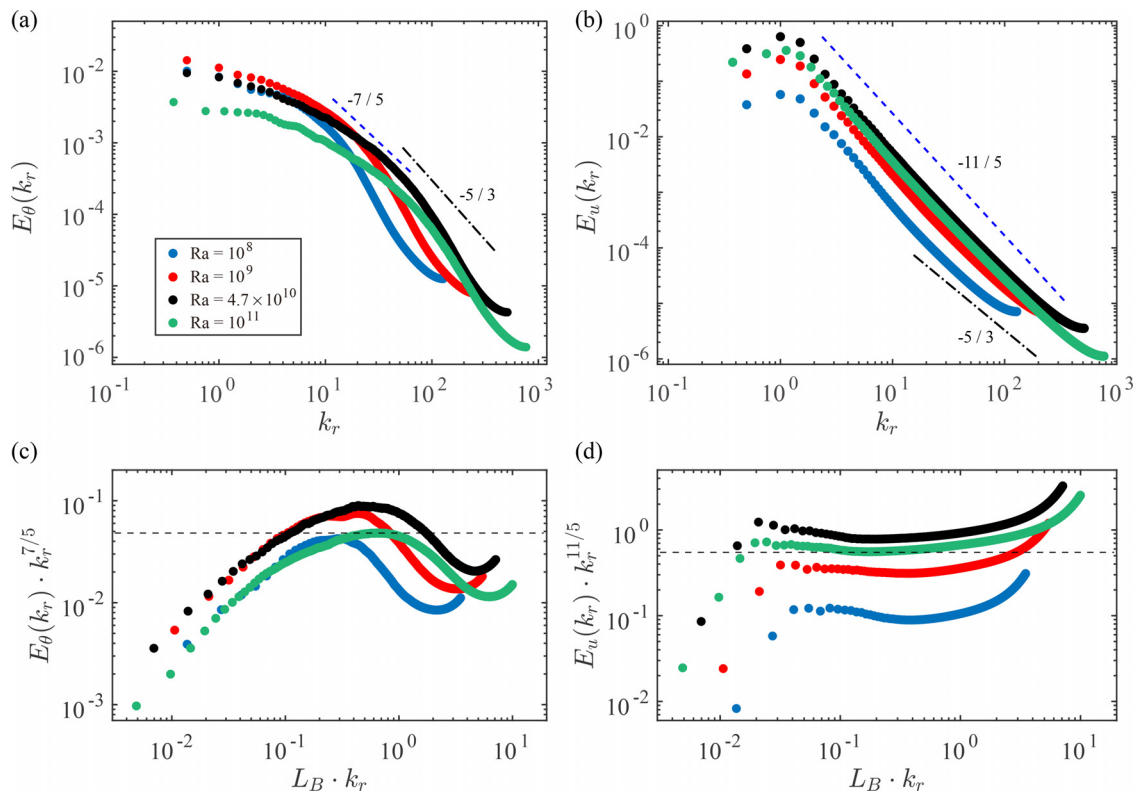


FIG. 5. (a) Temperature power spectra $E_\theta(k_r)$ as a function of the radial wavenumber k_r (out of the BLs) averaged axially, azimuthally, radially, and by time for different Ra. (b) Radial velocity power spectra $E_u(k_r)$ as a function of the radial wavenumber k_r (out of the BLs) averaged axially, azimuthally, radially, and by time for different Ra. [(c) and (d)] Compensated plot of [(a) and (b)] with the PS compensated by the BO59 scaling prediction, and the radial wavenumber k_r compensated by the Bolgiano scale L_B . The horizontal dashed lines mark the BO59 scaling. All fractions are the slopes of the nearby reference lines.

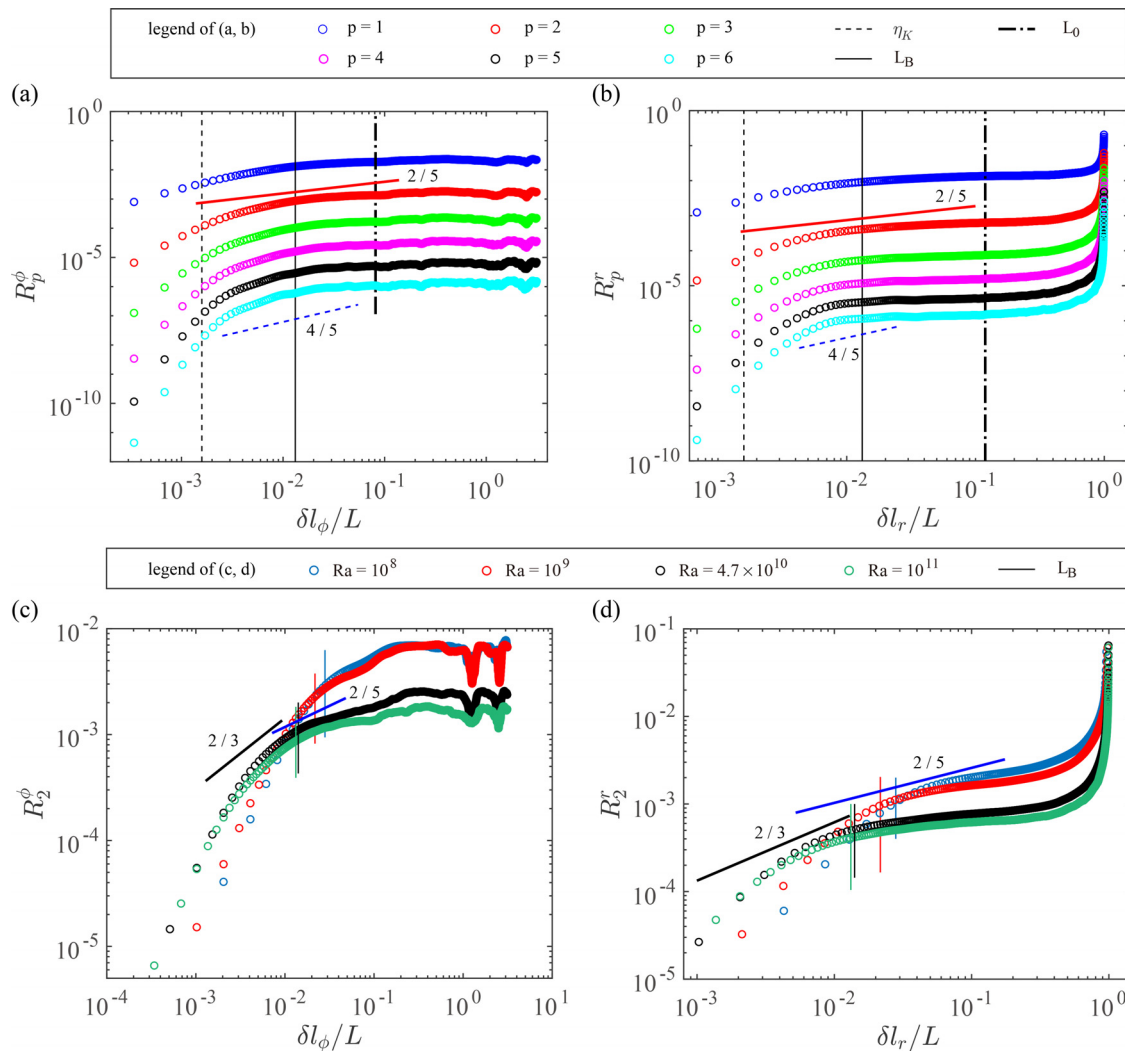


FIG. 6. Temperature structure functions taken at $Ra = 10^{11}$ (a) calculated in the azimuthal direction (at $R' = 0.15$, out of the BL) averaged axially, azimuthally, and by time and (b) calculated in the radial direction (except the BLs region) averaged axially, azimuthally, radially, and by time. The order p increases from 1 to 6 from top to bottom. The second-order temperature SFs (c) calculated in the azimuthal direction and (d) radial direction for different Ra . The fractions are the slopes of the nearby reference lines. The integral lengths, Bolgiano lengths, and Kolmogorov lengths are indicated with the dash-dotted lines, the solid lines, and the dashed lines, respectively.

sixth-order temperature SFs is still relatively flat, implying the energy cascade might not occur at the scales much larger than L_B . For $\eta_K \lesssim \delta l \lesssim L_B$, the slopes from the third to sixth-order SFs are similar. For classical RB^{71,72} and some other buoyancy-driven turbulence,^{63,73} the exponents of temperature SFs are also observed to increase extremely slowly with order p and the saturated exponent ξ_∞^θ is around 0.8. Zhou and Xia⁷² considered that the saturation is related to thermal plumes. Here, we note that in supergravitational turbulence, ξ_∞^θ for temperature SFs in the azimuthal direction agrees with the value of 4/5 found in classical RB turbulence [see Fig. 6(a)]. For the second-order temperature SFs, it is found that the BO59-like scalings (2/5) are around L_B for each Ra [see Figs. 6(c) and 6(d)]. Furthermore, we identify a potential scaling range for the radial temperature SF [Fig. 6(d)] at $\delta l_r/L \simeq 10^{-1}$ showing a slope $< 2/5$. The fitting scaling

exponents for this range are $\simeq 0.1$ for $Ra = [4.7 \times 10^{10}, 10^{11}]$ and $\simeq 0.2$ for $Ra = [10^8, 10^9]$.

As shown in Figs. 6(c) and 6(d), the amplitude of the second-order temperature SFs increases with Ra for $\delta l \lesssim 10^{-2}$, while the amplitude decreases with the increase in Ra for $\delta l \gtrsim 10^{-2}$. As Ra increases, thermal BLs become thinner due to the stronger shear effects of the LSC [see Fig. 7(d)]. Here, we adopt the slope method^{24,74} to calculate the thermal BL thickness $(\lambda_t)_s$ as the distance where the tangent of the temperature profile at the cylindrical wall intersects the bulk temperature. The result of $(\lambda_t)_s$ is basically consistent with that of $(\lambda_t)_{Nu} \equiv L/(2Nu)$ estimated by Nusselt number^{9,75} for different Ra . The scaling exponent 0.29 is similar to the thermal BL thickness in traditional RBC.^{76,77} The detaching thermal plumes are considered as parts of the thermal BLs,^{78,79} so the scale of plumes is smaller with

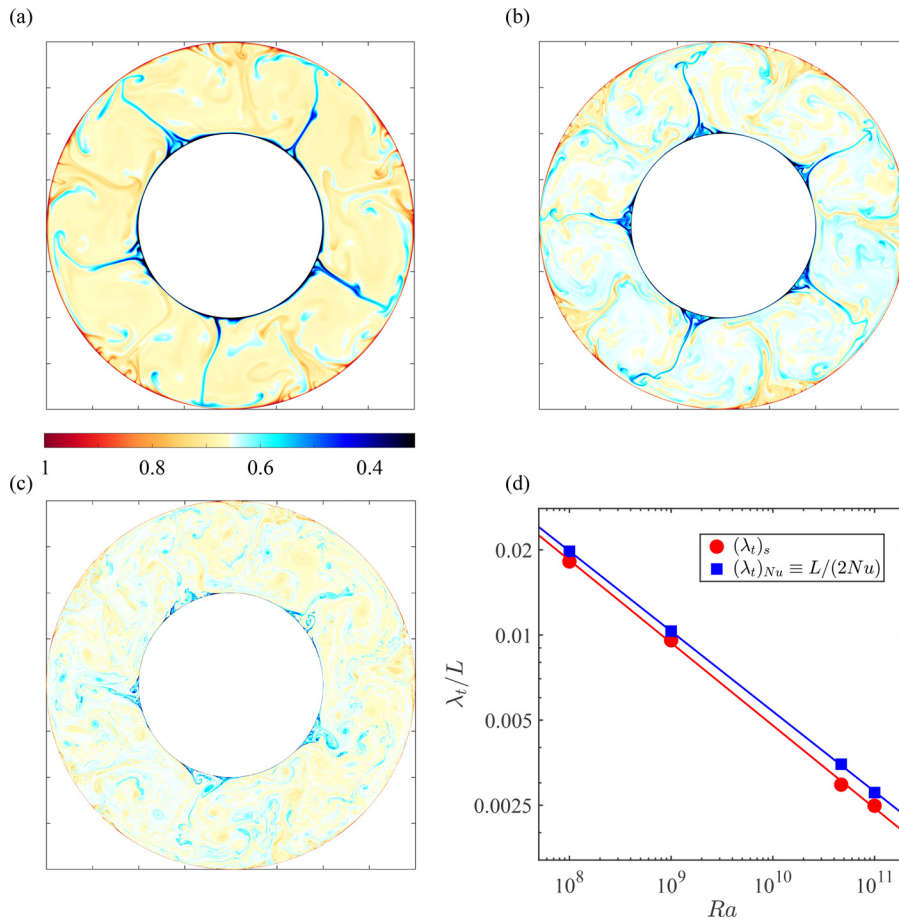


FIG. 7. Instantaneous temperature fields at the mid-axial height for (a) $Ra = 10^8$, (b) $Ra = 10^9$, and (c) $Ra = 10^{11}$. [(a)–(c)] share the same colorbar from 0.3 to 1. (d) The thermal BL thickness calculated from the slope method $(\lambda_t)_s$ ^{24,74} and Nusselt number $(\lambda_t)_{Nu}$ ^{9,75} as a function of Ra . The fitted lines are $(\lambda_t)_s = 3.99Ra^{-0.29 \pm 0.02}$ and $(\lambda_t)_{Nu} = 3.66Ra^{-0.28 \pm 0.01}$.

increasing Ra [Figs. 7(a)–7(c)]. Since thermal plumes are dominant carriers of heat in turbulent convection,⁸⁰ the smaller scale of plumes represents the amplitude of temperature increment becomes weaker for large scales and stronger for small scales.

Next, we consider the radial velocity SFs (Fig. 8), which exhibit relatively longer BO59-like scaling ranges than the temperature SFs. The transverse integral scales $(L_0)_{azi}$ and longitudinal integral scales $(L_0)_{rad}$ (Table II) are calculated by integrating the transverse and longitudinal autocorrelation functions of the radial velocity u_r , respectively.⁷⁰ BO59-like scalings are observed between L_B and $(L_0)_{azi}$ for the transverse SFs of u_r [Figs. 8(a) and 8(c)], while it is found near the integral scale $(L_0)_{rad}$ for the longitudinal SFs [Figs. 8(b) and 8(d)]. Kunnen *et al.*²⁶ reported that the local Bolgiano scale can be about one order of magnitude larger than the global Bolgiano scale, so BO59 scalings appearing at the scale larger than the global L_B is possible for the longitudinal SFs. As shown in Table II, it is found that the longitudinal integral length scale $(L_0)_{rad}$ is larger [for isotropic turbulence this can be quantified: $(L_0)_{rad} = 2(L_0)_{azi}$ ⁷⁰]. Thus a longer scaling range exists between L_B and $(L_0)_{rad}$, in comparison with its transverse counterpart, leading to its detection easier. To obtain high-order SFs with good statistics, the transverse SFs are averaged axially, azimuthally, and by time, and the longitudinal SFs are averaged in the radial direction

additionally. We examine the convergence carefully while computing the SFs, which is generally verified by the integral kernels,^{81–85}

$$F(\Delta_{\phi,r}u_r) \times |\Delta_{\phi,r}u_r|^p, \quad (7)$$

where $\Delta_{\phi,r}u_r$ denotes the increments of the radial velocity in the azimuthal or the radial direction. $F(\Delta_{\phi,r}u_r)$ is the probability density function of the velocity increments. Convergence for high-order SFs is more severe.^{81,84,86,87} As shown in the inset of Figs. 8(a) and 8(b), we plot the integral kernels of SFs at the Bolgiano lengths for $p = 6$. It is indicated that the tails of the integral kernels are converged basically, thus we have sufficient statistics to capture all the rare events necessary to faithfully calculate the SFs. As shown in Figs. 8(e) and 8(f), the second-order SFs show the predicted BO59-like scaling for $Ra \in [10^8, 10^{11}]$ and the BO59-like scaling ranges fall in $\delta l \gtrsim L_B$. In addition, we show that the amplitudes of transverse and longitudinal SFs increase with Ra , thus exhibiting stronger nonlinearity for flows with larger Ra .⁶⁷

As the scaling is obvious for the SFs of the radial velocity [Figs. 8(c) and 8(d)], power-law fittings in the range $L_B \leq \delta l_\phi \leq 5L_B$ for the transverse SFs and $L_B \leq \delta l_r \leq 30L_B$ for the longitudinal SFs are performed. The SF exponents as a function of the order p for $Ra = 4.7 \times 10^{10}$ and 10^{11} are shown in Fig. 9. The error bars are from

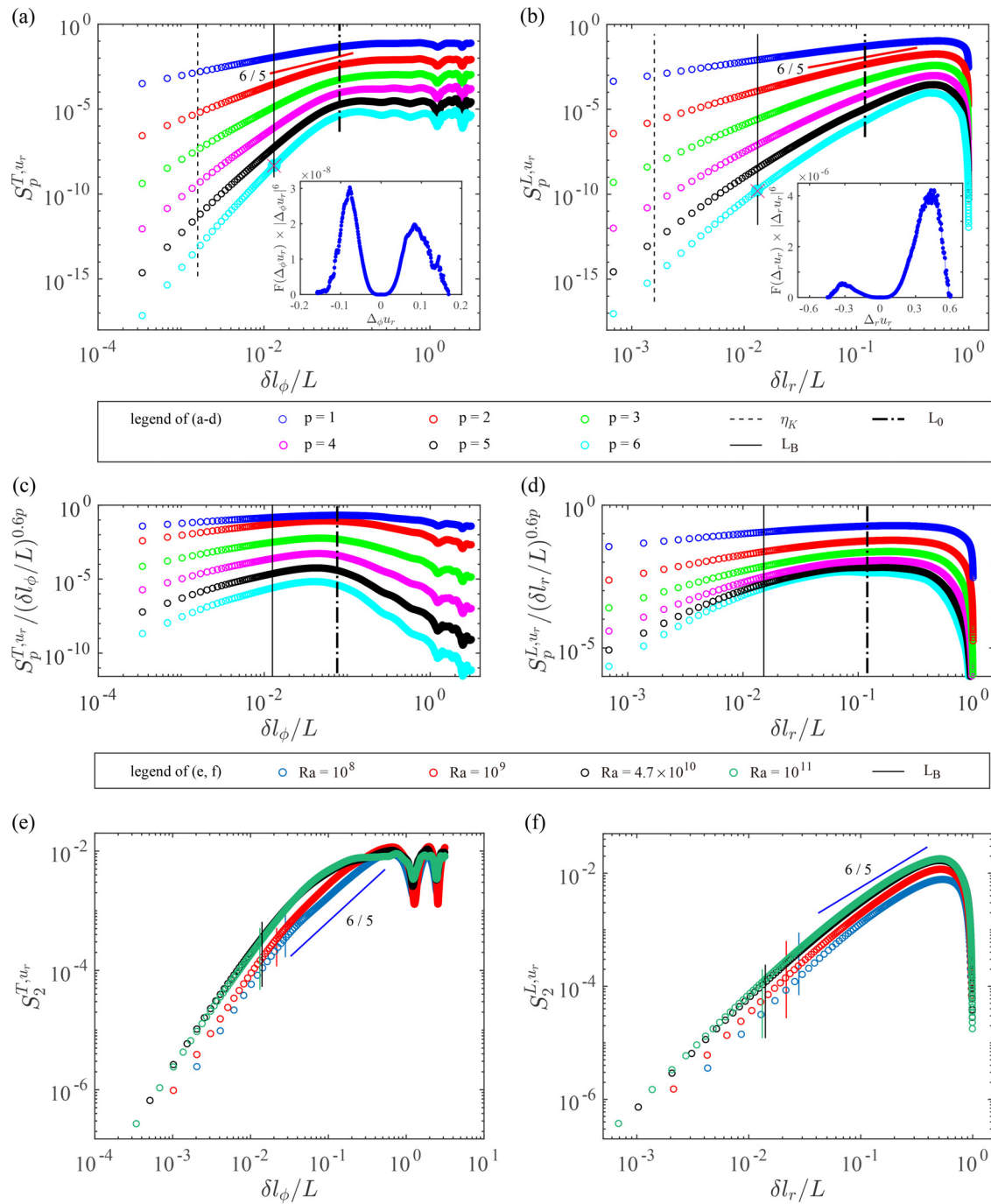


FIG. 8. Structure functions of the radial velocity taken at $Ra = 10^{11}$ (a) calculated in the azimuthal direction (at $R' = 0.15$, out of the BL) averaged axially, azimuthally, and by time and (b) calculated in the radial direction (except the BLs region) averaged axially, azimuthally, radially, and by time. The order p increases from 1 to 6 from top to bottom. Inset of [(a) and (b)]: Integral kernels of SF at the Bolgiano lengths for $p = 6$ (denoted by the red cross in the sixth-order SFs). [(c) and (d)] are the same data as [(a) and (b)] but S_p^{T,u_r} and S_p^{L,u_r} are compensated by BO59 scaling $(\delta l)^{0.6p}$, respectively. For the sake of clarity, the third- to sixth-order transverse SFs in (c) have been shifted down by 0.1 with respect to its higher neighbor. The second-order SFs of the radial velocity (e) calculated in the azimuthal direction and (f) calculated in the radial direction for different Ra . The fractions are the slopes of the nearby reference lines. In [(a)–(d)], the integral lengths, Bolgiano lengths, and Kolmogorov lengths are indicated with the dash-dotted lines, the solid lines, and the dashed lines, respectively. In (e) and (f), the Bolgiano lengths are indicated by the vertical solid lines.

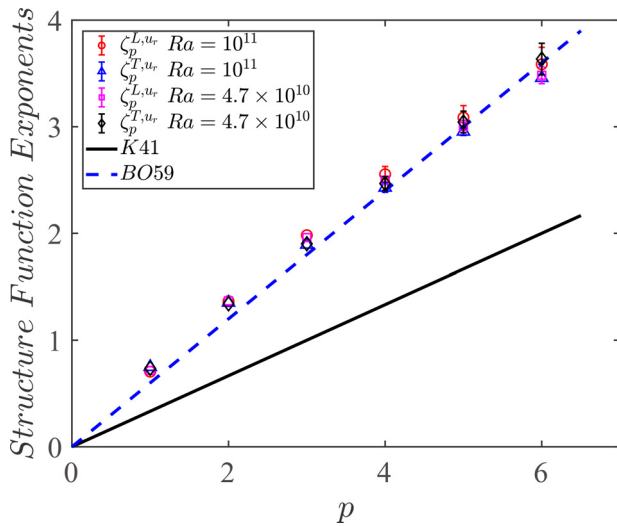


FIG. 9. Comparison of radial velocity SF exponents at $Ra = 10^{11}$ and 4.7×10^{10} with the model predictions. ζ_p^L and ζ_p^T are the scaling exponents of the p th-order longitudinal and transverse SFs of the radial velocity u_r , respectively. The power-law fitting ranges are $L_B \leq \delta l_\phi \leq 5L_B$ for the transverse SFs and $L_B \leq \delta l_r \leq 30L_B$ for the longitudinal SFs. The solid line is the prediction of K41 $\zeta_p = p/3$. The dashed line corresponds to the prediction of BO59 for the velocity $\zeta_p = 3p/5$. The error bars are from the difference of the SF exponents fittings for the first half and the second half of the averaging time.

the difference of the fittings for the first half and second half of the averaging time. The error is small and the maximum error is ± 0.12 corresponding to the sixth-order transverse SF at $Ra = 4.7 \times 10^{10}$. The data coincide with the theoretical prediction of BO59-like scaling $\zeta_p^u \sim 3p/5$ (the dashed line) basically and small deviations probably result from the contamination of the fitting by the non-BO59 range, while the data deviate from the K41 scaling $\zeta_p^u \sim p/3$ (the solid line) significantly. For high Ra , the flow is driven by the large centrifugal

buoyancy in the radial direction. So both the transverse and longitudinal SFs of the radial velocity u_r show BO59-like scaling. In addition, intermittency corrections for the velocity field are weak and within the errorbars, which are also observed in some two-dimensional (2D) turbulence.^{63,88} As the flow in ACRBC is quasi-2D, the mechanism for the energy cascade is probably similar to 2D turbulence.

C. Statistics of temperature fluctuations in different regions

In order to gain a deeper insight into the physics behind the small-scale properties in this novel turbulent flow system, we investigate probability density function (p.d.f.) of the temperature fluctuations $\delta\theta/\sigma_\theta$ in four different flow regions, where $\delta\theta(r, \phi, t) = \theta(r, \phi, t) - \langle \theta(r, \phi, t) \rangle_t$ and σ_θ is the root mean square (r.m.s.) value of $\delta\theta$. As shown in Fig. 10(b), we first identify the local strongest plumes according to the azimuthal temperature distribution at $R' = (r - R_i)/L = 0.2$ or $R' = 0.8$ at each time. The flow near this region is similar to the large-scale circulation (LSC) in traditional RBC. While we note that because the flow is strong due to the super-gravity, and Coriolis force can deflect the plumes, these “radial large-scale circulation” positions (ϕ_r) are not strict. Second, based on the spatial distribution of thermal plumes in the convection cell, the convective flow can be divided into four distinct regions, namely, turbulent bulk ($R' \in [1/3, 2/3]$ and $\phi \in [\phi_r/3, 2\phi_r/3]$), mixing zone ($R' \in [0.06, 0.3] \cup [1.7, 1.94]$ and $\phi \in [\phi_r/3, 2\phi_r/3]$), radial large-scale circulation region ($R' \in [0.1, 0.9]$ and $\phi \in [0, \phi_r/5] \cup [4\phi_r/5, \phi_r]$), and thermal BL ($R' \in [0.2\delta_{th}, 0.6\delta_{th}] \cup [1 - 0.6\delta_{th}, 1 - 0.2\delta_{th}]$), as shown in Fig. 10(a). Note that the criterion of the different regions is based on recent studies of temperature fluctuations in traditional RBC.^{89,90} Third, the space- and time-series of the temperature fluctuations $\delta\theta/\sigma_\theta$ in each region are extracted and used to calculate the p.d.f.s in each region and different Ra .

As shown in Fig. 11, except the thermal BL, the strength of the cold plumes is obviously larger than the hot plumes. Especially for the temperature fluctuations at $Ra = 10^{11}$ [Fig. 11(b)], the p.d.f.s in the

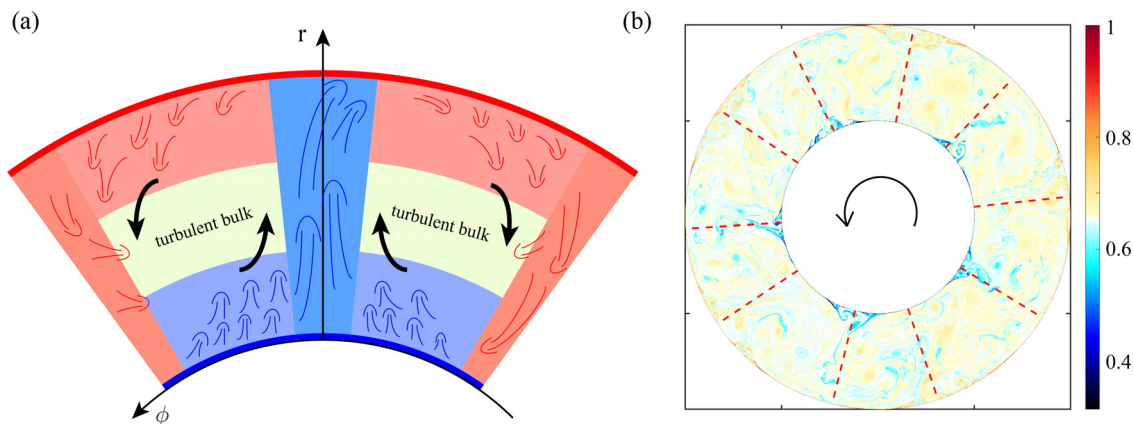


FIG. 10. (a) Sketch of a part of the system including a pair of convection rolls, which defines the distinct flow regions in ACRBC. The flow regions include the turbulent bulk region ($R' \in [1/3, 2/3]$ and $\phi \in [\phi_r/3, 2\phi_r/3]$), mixing zone ($R' \in [0.06, 0.3] \cup [1.7, 1.94]$ and $\phi \in [\phi_r/3, 2\phi_r/3]$), radial large-scale circulation region ($R' \in [0.1, 0.9]$ and $\phi \in [0, \phi_r/5] \cup [4\phi_r/5, \phi_r]$), and thermal boundary layer ($R' \in [0.2\delta_{th}, 0.6\delta_{th}] \cup [1 - 0.6\delta_{th}, 1 - 0.2\delta_{th}]$). The black arrows indicate the direction of the large-scale circulation. (b) Instantaneous temperature field at the mid-axial height for $Ra = 10^{11}$. The red dashed lines are the azimuthal positions of the radial large-scale circulation or the local strongest plumes. The arrow indicates that the system rotates anticlockwise. The colorbar is from 0.3 to 1.

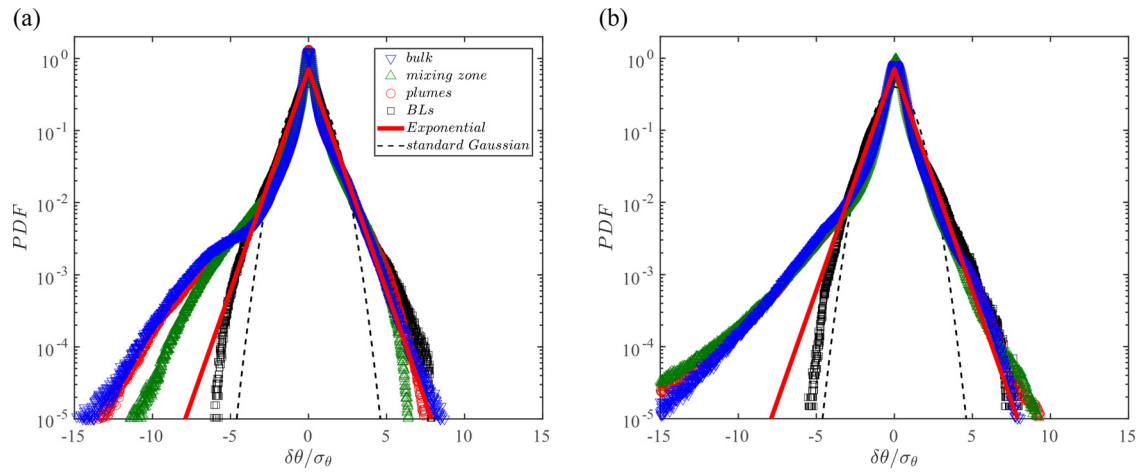


FIG. 11. The p.d.f.s of normalized temperature fluctuations $\delta\theta/\sigma_\theta$ in four different flow regions: bulk region, mixing zone, radial large circulation region, and thermal boundary layer region for (a) $Ra = 10^9$ and (b) $Ra = 10^{11}$. The four flow regions are shown and defined in Fig. 10. The black dashed lines show a standard Gaussian distribution $P(\delta\theta/\sigma_\theta) = \frac{1}{\sqrt{2\pi}} e^{-(\delta\theta/\sigma_\theta)^2/2}$ and the red solid lines show a plot of exponential distribution $P(\delta\theta/\sigma_\theta) = \frac{1}{\sqrt{2}} e^{-\sqrt{2}|\delta\theta/\sigma_\theta|}$.⁹¹

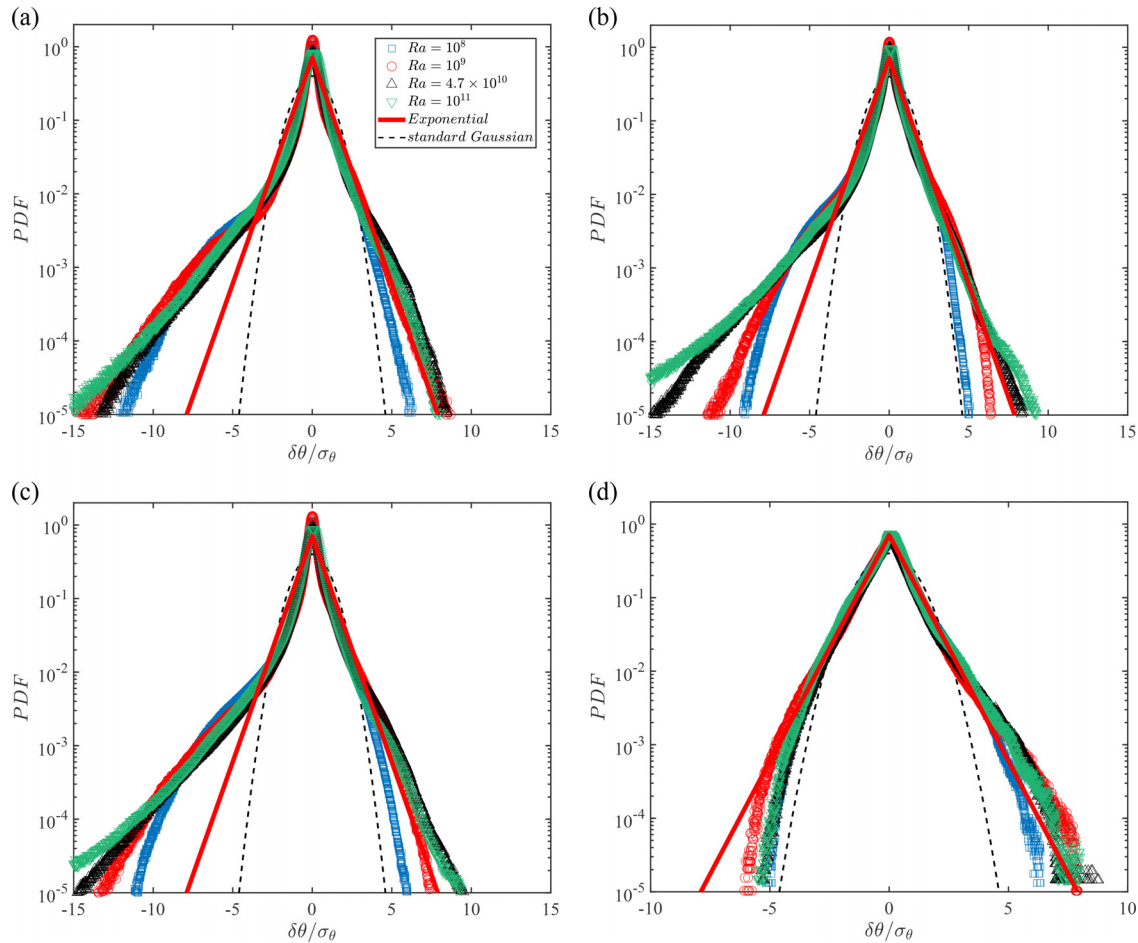


FIG. 12. The p.d.f.s of the temperature fluctuations $\delta\theta/\sigma_\theta$ normalized by the corresponding r.m.s. value for different Ra in four different flow regions: (a) bulk region, (b) mixing zone, (c) radial large scale circulation region, and (d) thermal boundary layer region. The four flow regions and coordinate system used are shown in Fig. 10. The black dashed lines show a standard Gaussian distribution $P(\delta\theta/\sigma_\theta) = \frac{1}{\sqrt{2\pi}} e^{-(\delta\theta/\sigma_\theta)^2/2}$, and the red solid lines show a plot of exponential distribution $P(\delta\theta/\sigma_\theta) = \frac{1}{\sqrt{2}} e^{-\sqrt{2}|\delta\theta/\sigma_\theta|}$.⁹¹

turbulent bulk, mixing zone, and radial large-scale circulation region are collapsed basically. The flow structures and statistics in the most of the flow regions tend to be similar to Ra increases, which may be due to the strong centrifugal buoyancy at high Ra in ACRBC. Note that in traditional RBC,^{89,90} it is found that the p.d.f.s of the temperature fluctuation $\delta\theta/\sigma_\theta$ are very different in these regions (see Fig. 4 of Wang *et al.*⁸⁹). Comparing the flow structure [Fig. 10(b)] in ACRBC with that in traditional RBC, the flow seems more homogeneous in ACRBC, which may lead to the assumption of BO59 scaling being more reasonable.²⁰ Note that the stronger cold plumes in different regions may facilitate the turbulent mixing.

From the p.d.f.s of the $\delta\theta/\sigma_\theta$ in the four different flow regions (Fig. 12), it is seen that the influence of Ra on the flow statistics in turbulent bulk [Fig. 12(a)], radial large-scale circulation region [Fig. 12(c)], and thermal BL [Fig. 12(d)] is relatively weak, while for the mixing zone [Fig. 12(b)], the p.d.f. becomes more asymmetric with increasing Ra, suggesting that there exist more and much stronger cold plumes at high Ra. We also note that the p.d.f.s of $\delta\theta/\sigma_\theta$ in the turbulent bulk are not the Gaussian distribution $P(\delta\theta/\sigma_\theta) = \frac{1}{\sqrt{2\pi}} e^{-(\delta\theta/\sigma_\theta)^2/2}$ and exponential distribution $P(\delta\theta/\sigma_\theta) = \frac{1}{\sqrt{2}} e^{-\sqrt{2}|\delta\theta/\sigma_\theta|}$ suggested by He *et al.*⁹¹ The strong centrifugal buoyancy and turbulent mixing resulting from the many strong cold plumes in ACRBC might be the reason for the BO59-like scalings in some of the PS and SFs.

IV. DISCUSSION

In ACRBC, BO59-like scaling is found, which may result from the large supergravity. The scale dependence of kinetic energy supplied by centrifugal buoyancy ($\alpha\omega^2 R\theta u$) might be different from traditional RBC because of the supergravity in ACRBC. In experiments, an effective gravity of 100 times Earth's gravity can be achieved.²⁵ The large centrifugal buoyancy mainly results in more stronger cold plumes at high Ra. The universal shape of the PDF in different flow regions at high Ra suggests that the flow dynamics in most regions of ACRBC are similar, which is significantly different from traditional RBC. The stronger turbulent-mixing and larger buoyancy force (more and stronger cold plumes) in ACRBC may result in the wider BO59-like scaling range with the increase in Ra. We should note that Coriolis force appears in this new convection system. On the one hand, Coriolis force leads to the quasi-2D flow state according to the Taylor–Proudman theorem. On the other hand, the deflected plumes can break through the “sidewall” existed in traditional RBC, which might lead to the larger azimuthal integral scale in ACRBC than traditional RBC and longer BO59-like scaling regime. In the present study, we conduct a set of quasi-2D DNS. Inverse energy cascade occurs in 2D turbulence.^{73,88,92} In buoyancy-driven 2D turbulence, Zhou *et al.*⁶⁴ found that the kinetic energy, injected by buoyancy term also cascades upward to larger scales and follows the BO59 scaling. The analyses of the scale-by-scale balance and energy flux need to be further studied. Furthermore, BO59-like scaling may be identified in a large aspect ratio and no sidewalls cell as suggested by Kunnen *et al.*²⁶ The mean aspect ratio of ACRBC is $\bar{\Gamma}_\parallel = \pi(R_o + R_i)/L \approx 9.42$. A larger azimuthal length compared to the Bolgiano scale can result in a longer scaling range. As no sidewall exists in the azimuthal direction and periodic boundary conditions are adopted in the axial direction, the effects due to proximity of the sidewalls can be avoided. Additionally, we notice that Bhattacharya

*et al.*⁶⁷ studied the Pr dependence of the spectra in traditional RBC at $Ra = 10^7$. They found Kolmogorov scalings for $Pr \leq 1$ and a much steeper energy spectrum $E_u(k) \sim k^{-3.49}$ for $Pr = 6.8$. Note that the scaling -3.49 is significantly different from the BO59 scaling -2.2 . So it is considered that BO59-like scalings found in ACRBC are not consequences of Pr effects.

V. CONCLUSION

We present an analysis of the power spectra and structure functions in annular centrifugal Rayleigh–Bénard Convection, by means of quasi-2D DNS, with Ra varying from 10^8 to 10^{11} , and Pr, Ro^{-1} , η fixed at 10.7, 16, 0.5, respectively. First, BO59-like scaling $E_\theta(k) \sim k^{-7/5}$ for the thermal spectrum in the azimuthal direction and $E_u(k) \sim k^{-11/5}$ for the energy spectrum in both the azimuthal and radial directions are observed. Especially, for the radial velocity PS calculated in the radial direction, BO59-like scaling is identified for each Ra, and the scaling range spans nearly two decades for $Ra = 10^{11}$, which implies centrifugal buoyancy may play an important role in the energy cascade process. Furthermore, it is found that the width of the wavenumber range over which BO59-like scaling is observed increases with Ra, which suggests the Bolgiano scale L_B decreases with the increase in Ra. Second, temperature and velocity SFs are investigated. The exponents of temperature SFs are observed to saturate from third to sixth-order SFs, which agrees with the results in classical RBC and Rayleigh–Taylor turbulence basically. In addition, since the scale of plumes becomes smaller with the increase in Ra, the amplitudes of the temperature SFs increase for small scales and decrease for large scales. Similar to the velocity PS, the radial velocity SFs follow the BO59-like scaling above the Bolgiano scale L_B . The amplitudes of velocity SFs increase with Ra, suggesting stronger nonlinearity for flows with larger Ra. The SF exponents as a function of the order p basically coincide with the theoretical prediction of BO59 scaling $\zeta_p^u \sim 3p/5$. Third, probability density functions of temperature fluctuations $\delta\theta/\sigma_\theta$ in different regions are studied systematically. It is found that the cold plumes are strong in ACRBC almost in all regions. The unified profile of the p.d.f.s at high Ra suggests that similar turbulent dynamics exist in different regions of ACRBC. The stronger turbulent-mixing and larger buoyancy force (more stronger cold plumes) in ACRBC may result in the wider BO59-like scaling than traditional RBC. Of course, more studies are needed to further verify the BO59-like scaling in thermal turbulence.

ACKNOWLEDGMENTS

This work was supported by the Natural Science Foundation of China under Grant Nos. 11988102, 91852202, 11825204, and 92052201, and the Tencent Foundation through the XPLOER PRIZE.

AUTHOR DECLARATIONS

Conflict of Interest

The authors have no conflicts to disclose.

DATA AVAILABILITY

The data that support the findings of this study are available from the corresponding author upon reasonable request.

APPENDIX: DERIVATION OF THE CORRECTION OF RADIUS RATIO $f(\eta)$

Below, we provide the detailed derivation of the correction of radius ratio $f(\eta)$ for the Bolgiano scale L_B and Kolmogorov scale η_K . First, the governing equations in dimensional form read as follows:

$$\vec{\nabla} \cdot \vec{u} = 0, \quad (\text{A1})$$

$$\frac{\partial \vec{u}}{\partial t} + (\vec{u} \cdot \vec{\nabla})\vec{u} = -\frac{1}{\rho}\vec{\nabla}p - 2\vec{\omega} \times \vec{u} + \nu\vec{\nabla}^2\vec{u} - \alpha\delta T\omega^2\vec{r}, \quad (\text{A2})$$

$$\frac{\partial T}{\partial t} + (\vec{u} \cdot \vec{\nabla})T = \kappa\vec{\nabla}^2T. \quad (\text{A3})$$

Here, $\delta T = T - T_0$ is the temperature difference from the reference temperature.

Second, we take the scalar product of Eq. (A2) with \vec{u} and the product of Eq. (A3) with T , and then average over the whole convective cell and time, and we obtain

$$\begin{aligned} \frac{1}{2} \frac{d}{dt} \langle \vec{u} \cdot \vec{u} \rangle_{V,t} + \frac{1}{2} \langle \vec{u} \cdot \vec{\nabla}(\vec{u} \cdot \vec{u}) \rangle_{V,t} \\ = -\langle \vec{u} \cdot \vec{\nabla}p \rangle_{V,t} + \nu \langle \vec{u} \cdot \vec{\nabla}^2\vec{u} \rangle_{V,t} - 2\langle \vec{\omega} \times \vec{u} \cdot \vec{u} \rangle_{V,t} \\ + \alpha\omega^2 \langle r u_r T \rangle_{V,t}, \end{aligned} \quad (\text{A4})$$

$$\frac{1}{2} \frac{d\langle T^2 \rangle_{V,t}}{dt} + \frac{1}{2} \langle \vec{u} \cdot \vec{\nabla}(T^2) \rangle_{V,t} = \kappa \langle \vec{\nabla} \cdot (T\vec{\nabla}T) \rangle_{V,t} - \kappa \langle |\vec{\nabla}T|^2 \rangle_{V,t}. \quad (\text{A5})$$

When the flow is in the stationary state, $d\langle \cdot \rangle_{V,t}/dt$ vanishes. Using the incompressibility condition Eq. (A1) and the no-slip boundary condition, Eqs. (A4) and (A5) become

$$\varepsilon_u = \nu \langle (\vec{\nabla} \times \vec{u})^2 \rangle_{V,t} = \alpha\omega^2 \langle r u_r T \rangle_{V,t}, \quad (\text{A6})$$

$$\varepsilon_\theta = \kappa \langle |\vec{\nabla}T|^2 \rangle_{V,t} = \kappa \langle \vec{\nabla} \cdot (T\vec{\nabla}T) \rangle_{V,t}, \quad (\text{A7})$$

where ε_u and ε_θ are the mean energy and thermal dissipation rate. Averaging Eq. (A3) azimuthally, axially, and temporally, we can deduce the Nusselt number Nu ,^{22,24}

$$\text{Nu} = \frac{J}{J_{\text{con}}} = \frac{\langle u_r T \rangle_{t,\phi,z} - \kappa \frac{\partial}{\partial r} \langle T \rangle_{t,\phi,z}}{\kappa \Delta (r \cdot \ln(\eta))^{-1}}. \quad (\text{A8})$$

Combining Eqs. (A6)–(A8) and the definition of Ra [Eq. (6)], we can obtain two exact relations for ACRBC,

$$\begin{aligned} \varepsilon_u &= \alpha\omega^2 \frac{1}{\pi(R_o^2 - R_i^2)H} \int_{R_i}^{R_o} 2\pi r H \langle r u_r T \rangle_{\phi,z,t} dr \\ &= \alpha\omega^2 \frac{1}{\pi(R_o^2 - R_i^2)H} \int_{R_i}^{R_o} 2\pi r H \left[\text{Nu} \kappa \Delta / \ln(\eta) + \kappa \left\langle r \frac{\partial T}{\partial r} \right\rangle_{\phi,z,t} \right] dr. \end{aligned}$$

To calculate the above integration, we estimate $\langle \frac{\partial T}{\partial r} \rangle_{\phi,z,t}$ by diffusive solution, i.e., $\langle \frac{\partial T}{\partial r} \rangle_{\phi,z,t} = -\frac{\Delta}{r \ln(\eta)}$. Then, we have

$$\begin{aligned} \varepsilon_u &= \frac{2\alpha\omega^2}{R_o^2 - R_i^2} \left[\frac{\text{Nu} \kappa \Delta}{\ln(\eta)} \int_{R_i}^{R_o} r dr - \kappa \int_{R_i}^{R_o} \frac{\Delta}{\ln(\eta)} r dr \right] \\ &= \frac{\alpha\omega^2 \kappa \Delta}{\ln(\eta)} (\text{Nu} - 1) \\ &= \frac{\kappa^2 \nu}{L^4} \text{Ra} (\text{Nu} - 1) \frac{2(\eta - 1)}{(1 + \eta) \ln(\eta)}. \end{aligned}$$

Similarly

$$\begin{aligned} \varepsilon_\theta &= \frac{\kappa}{\pi(R_o^2 - R_i^2)H} \left(2\pi R_o H \left\langle T \frac{\partial T}{\partial r} \right\rangle_{r=R_o} - 2\pi R_i H \left\langle T \frac{\partial T}{\partial r} \right\rangle_{r=R_i} \right) \\ &= \frac{\kappa}{\pi(R_o^2 - R_i^2)H} \left[2\pi R_o H \frac{\Delta}{2} \cdot \frac{Q}{2\pi R_o H \lambda} - 2\pi R_i H \left(-\frac{\Delta}{2} \right) \cdot \frac{Q}{2\pi R_i H \lambda} \right] \\ &= \frac{\kappa \Delta}{\pi(R_o^2 - R_i^2)H} \cdot \frac{Q}{\lambda} \\ &= \frac{\kappa \Delta}{\pi(R_o^2 - R_i^2)H} \cdot \text{Nu} \frac{\Delta 2\pi H}{\ln(\eta)} \\ &= \frac{\kappa \Delta^2 \text{Nu}}{L^2} \frac{2(\eta - 1)}{(1 + \eta) \ln(\eta)}, \end{aligned}$$

where Q is the heat input through the outer cylinder into the system per unit of time. Substitute the above expressions of ε_u and ε_θ into the Bolgiano scale L_B [Eq. (1)] and the Kolmogorov scale $\eta_K = \nu^{3/4}/\varepsilon_u^{1/4}$, we finally obtain

$$L_B = \frac{\text{Nu}^{1/2} L}{(\text{PrRa})^{1/4}} [f(\eta)]^{1/2}, \quad (\text{A9})$$

$$\eta_K = \frac{\text{Pr}^{1/2} L}{(\text{RaNu})^{1/4}} [f(\eta)]^{-1/4}, \quad (\text{A10})$$

where $f(\eta) = \frac{2(\eta-1)}{(1+\eta)\ln(\eta)}$. It is noted that for $\eta = 0.5$ (the present system), the corrections of radius ratio $[f(\eta)]^{1/2}$ and $[f(\eta)]^{-1/4}$ approximate to 1. Thus, the characteristic scales of ACRBC are very similar to those of traditional RBC.

REFERENCES

- Y. D. Afanasyev and Y. Zhang, "Cyclonic circulation of Saturn's atmosphere due to tilted convection," *Nat. Geosci.* **11**, 164–167 (2018).
- X. Tan, M. Lefèvre, and R. T. Pierrehumbert, "Convection modeling of pure-steam atmospheres," *Astrophys. J. Lett.* **923**(1), L15 (2021).
- L. Cheng, J. Abraham, Z. Hausfather, and K. E. Trenberth, "How fast are the oceans warming?," *Science* **363**, 128–129 (2019).
- Y. Yang, "Double diffusive convection in the finger regime for different Prandtl and Schmidt numbers," *Acta Mech. Sin.* **36**(4), 797–804 (2020).
- L. Fourel, A. Limare, C. Jaupart, E. Surducun, C. G. Farnetani, E. C. Kaminski, C. Neamtu, and V. Surducun, "The Earth's mantle in a microwave oven: Thermal convection driven by a heterogeneous distribution of heat sources," *Exp. Fluids* **58**, 90 (2017).
- M. Yoshida, "Dynamics of three-layer convection in a two-dimensional spherical domain with a growing innermost layer: Implications for whole solid-earth dynamics," *Phys. Fluids* **30**(9), 096601 (2018).
- C. Kang, A. Meyer, H. N. Yoshikawa, and I. Mutabazi, "Numerical study of thermal convection induced by centrifugal buoyancy in a rotating cylindrical annulus," *Phys. Rev. Fluids* **4**, 043501 (2019).
- J. Michael Owen and C. A. Long, "Review of buoyancy-induced flow in rotating cavities," *J. Turbomach.* **137**, 11 (2015).

- ⁹G. Ahlers, S. Grossmann, and D. Lohse, "Heat transfer and large scale dynamics in turbulent Rayleigh-Bénard convection," *Rev. Mod. Phys.* **81**, 503–537 (2009).
- ¹⁰X. Chen, D.-P. Wang, and H.-D. Xi, "Reduced flow reversals in turbulent convection in the absence of corner vortices," *J. Fluid Mech.* **891**, R5 (2020).
- ¹¹F. Chillà and J. Schumacher, "New perspectives in turbulent Rayleigh-Bénard convection," *Eur. Phys. J. E* **35**(7), 58 (2012).
- ¹²H. Liu, K. L. Chong, C. S. Ng, R. Verzicco, and D. Lohse, "Enhancing heat transport in multiphase Rayleigh-Bénard turbulence by changing the plate-liquid contact angles," *J. Fluid Mech.* **933**, R1 (2022).
- ¹³H. K. Pharesi, D. Kumar, K. Kumar, and J. K. Bhattacharjee, "Spectra and probability distributions of thermal flux in turbulent Rayleigh-Bénard convection," *Phys. Fluids* **28**(5), 055103 (2016).
- ¹⁴Z. Wang, V. Mathai, and C. Sun, "Self-sustained biphasic catalytic particle turbulence," *Nat. Commun.* **10**, 3333 (2019).
- ¹⁵H.-D. Xi and K.-Q. Xia, "Flow mode transitions in turbulent thermal convection," *Phys. Fluids* **20**(5), 055104 (2008).
- ¹⁶A. Xu, X. Chen, F. Wang, and H.-D. Xi, "Correlation of internal flow structure with heat transfer efficiency in turbulent Rayleigh-Bénard convection," *Phys. Fluids* **32**(10), 105112 (2020).
- ¹⁷A. Xu, B.-R. Xu, L.-S. Jiang, and H.-D. Xi, "Production and transport of vorticity in two-dimensional Rayleigh-Bénard convection cell," *Phys. Fluids* **34**(1), 013609 (2022).
- ¹⁸G. Xu, Q. Wang, Z. Wan, and D. Sun, "Heat transfer and plume statistics in turbulent thermal convection with sparse fractal roughness," *J. Hydrodyn.* **33**(5), 1065–1077 (2021).
- ¹⁹X. Zhu and Q. Zhou, "Flow structures of turbulent Rayleigh-Bénard convection in annular cells with aspect ratio one and larger," *Acta Mech. Sin.* **37**(8), 1291 (2021).
- ²⁰D. Lohse and K.-Q. Xia, "Small-scale properties of turbulent Rayleigh-Bénard convection," *Annu. Rev. Fluid Mech.* **42**(1), 335–364 (2010).
- ²¹M. K. Verma, A. Kumar, and A. Pandey, "Phenomenology of buoyancy-driven turbulence: Recent results," *New J. Phys.* **19**(2), 025012 (2017).
- ²²H. Jiang, X. Zhu, D. Wang, S. G. Huisman, and C. Sun, "Supergravitational turbulent thermal convection," *Sci. Adv.* **6**, eabb8676 (2020).
- ²³A. Rouhi, D. Lohse, I. Marusic, C. Sun, and D. Chung, "Coriolis effect on centrifugal buoyancy-driven convection in a thin cylindrical shell," *J. Fluid Mech.* **910**, A32 (2021).
- ²⁴D. Wang, H. Jiang, S. Liu, X. Zhu, and C. Sun, "Effects of radius ratio on annular centrifugal Rayleigh-Bénard convection," *J. Fluid Mech.* **930**, A19 (2022).
- ²⁵H. Jiang, D. Wang, S. Liu, and C. Sun, "Evidences existence ultimate regime supergravitational turbulent thermal convection," *arXiv:2110.01224* (2022).
- ²⁶R. P. J. Kunnen, H. J. H. Clercx, B. J. Geurts, L. J. A. van Bokhoven, R. A. D. Akkermans, and R. Verzicco, "Numerical and experimental investigation of structure-function scaling in turbulent Rayleigh-Bénard convection," *Phys. Rev. E* **77**, 016302 (2008).
- ²⁷D. Bohn, E. Deuker, R. Emunds, and V. Gorzelitz, "Experimental and theoretical investigations of heat transfer in closed gas-filled rotating annuli," *J. Turbomach.* **117**(1), 175–183 (1995).
- ²⁸F. Gao, J. W. Chew, and O. Marxen, "Inertial waves in turbine rim seal flows," *Phys. Rev. Fluids* **5**, 024802 (2020).
- ²⁹R. Hide and P. J. Mason, "Sloping convection in a rotating fluid," *Adv. Phys.* **24**(1), 47–100 (1975).
- ³⁰D. B. Pitz, J. W. Chew, and O. Marxen, "Effect of an axial throughflow on buoyancy-induced flow in a rotating cavity," *Int. J. Heat Fluid Flow* **80**, 108468 (2019).
- ³¹P. Vadasz, "Centrifugal buoyancy in a rotating fluid layer next to and distant from the rotation axis," *Phys. Fluids* **33**(3), 034123 (2021).
- ³²A. N. Kolmogorov, "The local structure of turbulence in incompressible viscous fluid for very large Reynolds numbers," *Dokl. Akad. Nauk SSSR* **30**, 9–13 (1941) [reprinted in *Proc. R. Soc. London, Ser. A* **434**, 9–13 (1991)].
- ³³A. M. Obukhov, "Structure of the temperature field in a turbulent flow," *Izv. Akad. Nauk SSSR, Ser. Geog. Geofiz.* **13**, 58 (1949).
- ³⁴S. Corrsin, "On the spectrum of isotropic temperature fluctuations in anisotropic turbulence," *J. Appl. Phys.* **22**, 469 (1951).
- ³⁵R. Bolgiano, "Turbulent spectra in a stably stratified atmosphere," *J. Geophys. Res.* **64**, 2226, <https://doi.org/10.1029/JZ064i012p02226> (1959).
- ³⁶A. M. Obukhov, "On the influence of hydrostatic forces on the structure of the temperature field turbulent flow," *Sov. Phys. Dokl.* **4**, 61 (1959).
- ³⁷A. S. Monin and A. M. Yaglom, "Locally isotropic turbulence," in *Statistical Fluid Mechanics* (The MIT Press, 1975), Chap. 8, pp. 387–393.
- ³⁸V. S. L'vov, "Spectra of velocity and temperature fluctuations with constant entropy flux of fully developed free-convective turbulence," *Phys. Rev. Lett.* **67**, 687 (1991).
- ³⁹V. Yakhot, "4/5 Kolmogorov law for statistically stationary turbulence: Application to high Rayleigh number Bénard convection," *Phys. Rev. Lett.* **69**, 769–771 (1992).
- ⁴⁰Y. Zhang, Q. Zhou, and C. Sun, "Statistics of kinetic and thermal energy dissipation rates in two-dimensional turbulent Rayleigh-Bénard convection," *J. Fluid Mech.* **814**, 165–184 (2017).
- ⁴¹Q. Zhou and L.-F. Jiang, "Kinetic and thermal energy dissipation rates in two-dimensional Rayleigh-Taylor turbulence," *Phys. Fluids* **28**(4), 045109 (2016).
- ⁴²D. Lohse, "Temperature spectra in shear flow and thermal convection," *Phys. Lett. A* **196**, 70 (1994).
- ⁴³A. Bershadskii, J. J. Niemela, A. Praskovsky, and K. R. Sreenivasan, "Clusterization and intermittency of temperature fluctuations in turbulent convection," *Phys. Rev. E* **69**, 056314 (2004).
- ⁴⁴L. Biferale and F. Toschi, "Anisotropies in homogeneous turbulence: Hierarchy of scaling exponents and intermittency of the anisotropic sectors," *Phys. Rev. Lett.* **86**, 4831 (2001).
- ⁴⁵G. I. Taylor, "The spectrum of turbulence," *Proc. R. Soc. London, Ser. A* **164**, 476 (1938).
- ⁴⁶X.-L. Qiu, S.-H. Yao, and P. Tong, "Large-scale coherent rotation and oscillation in turbulent thermal convection," *Phys. Rev. E* **61**, R6075–R6078 (2000).
- ⁴⁷Q. Zhou, C.-M. Li, Z.-M. Lu, and Y.-L. Liu, "Experimental investigation of longitudinal space-time correlations of the velocity field in turbulent Rayleigh-Bénard convection," *J. Fluid Mech.* **683**, 94–111 (2011).
- ⁴⁸Z. Song, W. Wang, N. Zhu, and X. Chao, "Gas velocimetry based on infrared laser-induced fluorescence," *Phys. Fluids* **33**(12), 125126 (2021).
- ⁴⁹C. Sun, Q. Zhou, and K.-Q. Xia, "Cascades of velocity and temperature fluctuations in buoyancy-driven thermal turbulence," *Phys. Rev. Lett.* **97**, 144504 (2006).
- ⁵⁰H.-Y. Zou, W.-F. Zhou, X. Chen, Y. Bao, J. Chen, and Z.-S. She, "Boundary layer structure in turbulent Rayleigh-Bénard convection in a slim box," *Acta Mech. Sin.* **35**, 713–728 (2019).
- ⁵¹X.-Z. Wu, L. Kadanoff, A. Libchaber, and M. Sano, "Frequency power spectrum of temperature-fluctuation in free-convection," *Phys. Rev. Lett.* **64**, 2140 (1990).
- ⁵²P. Tong and Y. Shen, "Relative velocity fluctuations in turbulent Rayleigh-Bénard convection," *Phys. Rev. Lett.* **69**, 2066 (1992).
- ⁵³S. Ashkenazi and V. Steinberg, "Spectra and statistics of velocity and temperature fluctuations in turbulent convection," *Phys. Rev. Lett.* **83**, 4760–4763 (1999).
- ⁵⁴E. S. C. Ching, "Intermittency of temperature field in turbulent convection," *Phys. Rev. E* **61**, R33–R36 (2000).
- ⁵⁵E. S. C. Ching, Y.-K. Tsang, T. N. Fok, X. He, and P. Tong, "Scaling behavior in turbulent Rayleigh-Bénard convection revealed by conditional structure functions," *Phys. Rev. E* **87**, 013005 (2013).
- ⁵⁶S. Cioni, S. Ciliberto, and J. Sommeria, "Temperature structure functions in turbulent convection at low Prandtl number," *Europhys. Lett.* **32**, 413–418 (1995).
- ⁵⁷V. Valori, A. Innocenti, B. Dubrulle, and S. Chibbaro, "Weak formulation and scaling properties of energy fluxes in three-dimensional numerical turbulent Rayleigh-Bénard convection," *J. Fluid Mech.* **885**, A14 (2020).
- ⁵⁸S.-Q. Zhou and K.-Q. Xia, "Scaling properties of the temperature field in convective turbulence," *Phys. Rev. Lett.* **87**, 064501 (2001).
- ⁵⁹E. S. C. Ching, "Scaling laws in the central region of confined turbulent thermal convection," *Phys. Rev. E* **75**, 056302 (2007).
- ⁶⁰T. Zürner, F. Schindler, T. Vogt, S. Eckert, and J. Schumacher, "Combined measurement of velocity and temperature in liquid metal convection," *J. Fluid Mech.* **876**, 1108–1128 (2019).

- ⁶¹D. Rosenberg, A. Pouquet, R. Marino, and P. D. Mininni, "Evidence for Bolgiano-Obukhov scaling in rotating stratified turbulence using high-resolution direct numerical simulations," *Phys. Fluids* **27**(5), 055105 (2015).
- ⁶²G. Boffetta and A. Mazzino, "Incompressible Rayleigh-Taylor turbulence," *Annu. Rev. Fluid Mech.* **49**(1), 119–143 (2017).
- ⁶³Q. Zhou, "Temporal evolution and scaling of mixing in two-dimensional Rayleigh-Taylor turbulence," *Phys. Fluids* **25**(8), 085107 (2013).
- ⁶⁴Q. Zhou, Y.-X. Huang, Z.-M. Lu, Y.-L. Liu, and R. Ni, "Scale-to-scale energy and enstrophy transport in two-dimensional Rayleigh-Taylor turbulence," *J. Fluid Mech.* **786**, 294–308 (2016).
- ⁶⁵Q. Zhou and K.-Q. Xia, "Disentangle plume-induced anisotropy in the velocity field in buoyancy-driven turbulence," *J. Fluid Mech.* **684**, 192–203 (2011).
- ⁶⁶M. Kaczorowski and K.-Q. Xia, "Turbulent flow in the bulk of Rayleigh-Bénard convection: Small-scale properties in a cubic cell," *J. Fluid Mech.* **722**, 596–617 (2013).
- ⁶⁷S. Bhattacharya, M. K. Verma, and R. Samtaney, "Prandtl number dependence of the small-scale properties in turbulent Rayleigh-Bénard convection," *Phys. Rev. Fluids* **6**, 063501 (2021).
- ⁶⁸R. Verzicco and P. Orlandi, "A finite-difference scheme for three-dimensional incompressible flows in cylindrical coordinates," *J. Comput. Phys.* **123**, 402–414 (1996).
- ⁶⁹R. Verzicco and R. Camussi, "Numerical experiments on strongly turbulent thermal convection in a slender cylindrical cell," *J. Fluid Mech.* **477**, 19–49 (2003).
- ⁷⁰S. B. Pope, "The scales of turbulent motion," in *Turbulent Flows* (Cambridge University Press, 2000), Chap. 6, pp. 196–197.
- ⁷¹A. Celani, T. Matsumoto, A. Mazzino, and M. Vergassola, "Scaling and universality in turbulent convection," *Phys. Rev. Lett.* **88**, 054503 (2002).
- ⁷²S.-Q. Zhou and K.-Q. Xia, "Plume statistics in thermal turbulence: Mixing of an active scalar," *Phys. Rev. Lett.* **89**, 184502 (2002).
- ⁷³X. Q. He, A. D. Bragg, Y. L. Xiong, and P. Fischer, "Turbulence and heat transfer on a rotating, heated half soap bubble," *J. Fluid Mech.* **924**, A19 (2021).
- ⁷⁴Q. Zhou and K.-Q. Xia, "Measured instantaneous viscous boundary layer in turbulent Rayleigh-Bénard convection," *Phys. Rev. Lett.* **104**, 104301 (2010).
- ⁷⁵X. He, E. Bodenschatz, and G. Ahlers, "Universal scaling of temperature variance in Rayleigh-Bénard convection near the transition to the ultimate state," *J. Fluid Mech.* **931**, A7 (2022).
- ⁷⁶R. Du Puits, C. Resagk, A. Tilgner, F. H. Busse, and A. Thess, "Structure of thermal boundary layers in turbulent Rayleigh-Bénard convection," *J. Fluid Mech.* **572**, 231–254 (2007).
- ⁷⁷R. S. Long, J. E. Mound, C. J. Davies, and S. M. Tobias, "Thermal boundary layer structure in convection with and without rotation," *Phys. Rev. Fluids* **5**, 113502 (2020).
- ⁷⁸S. Grossmann and D. Lohse, "Scaling in thermal convection: A unifying theory," *J. Fluid Mech.* **407**, 27–56 (2000).
- ⁷⁹S. Grossmann and D. Lohse, "Fluctuations in turbulent Rayleigh-Bénard convection: The role of plumes," *Phys. Fluids* **16**(12), 4462–4472 (2004).
- ⁸⁰X.-D. Shang, X.-L. Qiu, P. Tong, and K.-Q. Xia, "Measured local heat transport in turbulent Rayleigh-Bénard convection," *Phys. Rev. Lett.* **90**, 074501 (2003).
- ⁸¹F. Anselmetti, Y. Gagne, E. J. Hopfinger, and R. A. Antonia, "High-order velocity structure functions in turbulent shear flows," *J. Fluid Mech.* **140**, 63–89 (1984).
- ⁸²C. Meneveau and K. R. Sreenivasan, "The multifractal nature of turbulent energy dissipation," *J. Fluid Mech.* **224**, 429–484 (1991).
- ⁸³K. R. Sreenivasan, "Fractals and multifractals in fluid turbulence," *Annu. Rev. Fluid Mech.* **23**(1), 539–604 (1991).
- ⁸⁴K. R. Sreenivasan, R. A. Antonia, and H. Q. Danh, "Temperature dissipation fluctuations in a turbulent boundary layer," *Phys. Fluids* **20**(8), 1238–1249 (1977).
- ⁸⁵G. Stolovitzky, P. Kailasnath, and K. R. Sreenivasan, "Refined similarity hypotheses for passive scalars mixed by turbulence," *J. Fluid Mech.* **297**, 275–291 (1995).
- ⁸⁶S. G. Huisman, D. Lohse, and C. Sun, "Statistics of turbulent fluctuations in counter-rotating Taylor-Couette flows," *Phys. Rev. E* **88**, 063001 (2013).
- ⁸⁷S. B. Pope, "PDF methods," in *Turbulent Flows* (Cambridge University Press, 2000), pp. 463–475, Chap. 12.
- ⁸⁸G. Boffetta, A. Celani, and M. Vergassola, "Inverse energy cascade in two-dimensional turbulence: Deviations from Gaussian behavior," *Phys. Rev. E* **61**, R29–R32 (2000).
- ⁸⁹Y. Wang, X. He, and P. Tong, "Turbulent temperature fluctuations in a closed Rayleigh-Bénard convection cell," *J. Fluid Mech.* **874**, 263–284 (2019).
- ⁹⁰Y. Wang, Y. Wei, P. Tong, and X. He, "Collective effect of thermal plumes on temperature fluctuations in a closed Rayleigh-Bénard convection cell," *J. Fluid Mech.* **934**, A13 (2022).
- ⁹¹X. He, Y. Wang, and P. Tong, "Dynamic heterogeneity and conditional statistics of non-Gaussian temperature fluctuations in turbulent thermal convection," *Phys. Rev. Fluids* **3**, 052401 (2018).
- ⁹²R. H. Kraichnan, "Inertial ranges in two-dimensional turbulence," *Phys. Fluids* **10**(7), 1417–1423 (1967).